

# Stellar Populations of Globular Clusters in the Elliptical Galaxy NGC 1407

A. Javier Cenarro <sup>1,2</sup> and Michael A. Beasley <sup>2</sup>

*Instituto de Astrofísica de Canarias, La Laguna, 38200, Canary Islands, Spain*

[cenarro@iac.es](mailto:cenarro@iac.es)

Jay Strader and Jean P. Brodie

*Lick Observatory, University of California, CA 95064, USA*

and

Duncan A. Forbes

*Centre for Astrophysics & Supercomputing, Swinburne University, Hawthorn VIC 3122,  
Australia*

## ABSTRACT

We present high-quality, Keck spectroscopic data for a sample of 20 globular clusters (GCs) in the massive E0 galaxy NGC 1407. A subset of twenty line-strength indices of the Lick/IDS system have been measured for both the GC system and the central integrated star-light of the galaxy. Ages, metallicities and  $[\alpha/\text{Fe}]$  ratios have been derived using several different approaches. The majority GCs in NGC 1407 studied are old, follow a tight metallicity sequence reaching values slightly above solar, and exhibit mean  $[\alpha/\text{Fe}]$  ratios of  $\sim 0.3$  dex. In addition, three GCs are formally derived to be young ( $\sim 4$  Gyr), but we argue that they are actually old GCs hosting blue horizontal branches. We report, for the first time, evidence for the existence of two chemically-distinct subpopulations of metal-rich (MR) GCs. We find some MR GCs exhibit significantly larger  $[\text{Mg}/\text{Fe}]$  and  $[\text{C}/\text{Fe}]$  ratios. Different star formation time-scales are proposed to explain the correlation between Mg and C abundances. We also find striking CN

---

<sup>1</sup>Also at Departamento de Física de la Tierra, Astronomía y Astrofísica II, Facultad de Físicas, Universidad Complutense de Madrid, 28040 Madrid, Spain

<sup>2</sup>Also at Lick Observatory, University of California, CA 95064, USA

overabundances over the entire GC metallicity range. Interestingly, the behavior of C and N in metal-poor (MP) GCs clearly deviates from the one in MR GCs. In particular, for MR GCs, N increases dramatically while C essentially saturates. This may be interpreted as a consequence of the increasing importance of the CNO cycle with increasing metallicity.

*Subject headings:* globular clusters: general — galaxies: clusters — galaxies: formation

## 1. Introduction

The formation of globular clusters (GCs) is thought to be linked to major episodes of star formation in the galaxies (e.g. Larson 1996; Elmegreen & Efremov 1997; Ashman & Zepf 2001). This fact is supported by the systematic detection of young, massive star clusters –presumably progenitors of present-day GCs– in nearby, massive star-forming regions in the Large Magellanic Cloud (van den Bergh 1994) and other galaxies like the Antennae (Whitmore & Schweizer 1995), NGC 1275 (Holtzman et al. 1992), NGC 1569 (Ho & Filippenko 1996) and NGC 7252 (Miller et al. 1997). Therefore, observations of extragalactic GCs are an essential tool to our understanding of how the main star formation episodes of their host galaxies took place.

One of the most striking observational keys on the current topic is the existence of bi-modal color distributions in the GC systems of most galaxies. This fact has been widely interpreted as an evidence for two distinct GC subpopulations –metal-rich (MR; red) and metal-poor (MP; blue), qualitatively resembling the two GC subpopulations of spectroscopically-confirmed, different metallicities in our Galaxy–, although in the recent work of Yoon, Yi & Lee (2006) it is proposed that such a bimodality could instead be driven by non-linearities in the color-metallicity relationship. It is therefore clear that, if GC metallicity subpopulations indeed exist –see e.g. Strader, Brodie & Beasley (2007) for NGC 4472–, any convincing galaxy formation scenario must be able to reproduce such a common phenomenon.

In this sense, three GC formation scenarios have been proposed so far to explain the existence of GC subpopulations. In the *major merger* model (Ashman & Zepf 1992; Zepf & Ashman 1993), Es might be the by-product of wet (gas-rich) mergers of spiral galaxies (Toomre & Toomre 1972; Toomre 1977) with MR GCs being formed during the merger process (Schweizer 1987), whereas the MP GC subpopulation would be donated by the merging spirals. The *in-situ* scenario (Forbes et al. 1997) considers that the whole GC population was formed within the host galaxy during a multi-phase dissipational collapse.

Bimodality arises as MP GCs would form at a very early epoch whilst, after a dormant period of GC formation, MR GCs would form slightly later along with the bulk of the galaxy stars. Feedback processes (Forbes et al. 1997) and cosmic reionization (Santos 2003) have been proposed as potential candidates to justify the truncation of GC formation. Finally, based on the well-known relationship between the mean metallicity of the GC system and the mass of the host galaxy (Brodie & Huchra 1991), the *accretion* scenario (Côté, Marzke & West 1998; Côté et al. 2000; Côté, West & Marzke 2002) relies on the assumption that the MR GC subpopulation was formed within a massive, seed, host galaxy whereas MP GCs were acquired as a consequence of the accretion of their low-mass, host galaxies.

An essential prediction of the above GC formation scenarios deals with the ages of both GC subpopulations. In all cases, the MP GC subpopulation is predicted to be old. In the *major merger* model, the MR GC subpopulation is supposed to have the same age as that of the main merger driving their formation. The *in-situ/multiphase* scenario predicts MR GCs to be just slightly younger (by  $\sim 2 - 3$  Gyr) than MP GCs, whereas no systematic age differences between GC subpopulations are predicted by the accretion picture, as both MP and MR GCs would originally form at high redshift in their respective host galaxies before the accretion processes take place. Trying to determine whether systematic differences in the ages of GC subpopulations exist is, therefore, a crucial test to constrain the reliability of the different GC formation scenarios.

As a consequence, during the last two decades there has been a large effort to characterize the global properties and stellar populations of extragalactic GCs. The arrival of 8 - 10 m class telescopes has made it possible to extend studies of GCs to a wide variety of galaxy types, including massive ellipticals (Es), S0s, spiral galaxies and dwarf Es (dEs). We refer the reader to Brodie & Strader (2006) for a thorough review of the present status of extragalactic GCs and their implications for the current scenarios of galaxy formation and assembly. Overall, most GCs in all types of galaxies seem to be *old*, although it is worth noting that age-dating extragalactic GCs is unavoidably subject to the poor age-disentangling power of single stellar population (SSP) model predictions at the old regime.

In fact, all the above scenarios of GC formation may probably be valid to some extent: there exist evidences for the existence of young GCs in the *merger* remnant elliptical NGC 3610 (Strader et al. 2004), as well as hints for *accreted*, Galactic GCs (hereafter GGCs) associated to the streams of Sagittarius (Layden & Sarajedini 2000; Bellazzini et al. 2003a,b) and Fornax-Leo-Sculptor (Majewski 1994). Therefore, rather than questioning the reliability of the three different scenarios, the debate should be focused on determining the one that governs the formation of the bulk of GCs in the Universe. In practice, answering this question might not be so immediate either as the observational constrains of the different scenarios

would have blurred if they had happened at high redshift. In this sense, on the basis of the semi-analytic galaxy formation model by Cole et al. (2000), Beasley et al. (2002) adopted some elements of the three classic scenarios to study GC bimodality in a hierarchical galaxy formation context. More recently, supported by the old ages inferred from direct comparison with GGCs for a high-quality, spectroscopic subsample of GCs in eight Es, Strader et al. (2005) proposed a new GC formation picture that synthesizes aspects of both accretion and in-situ approaches in the context of galaxy formation through hierarchical merging at high-redshift (see also Rhode et al. 2005). Nevertheless, the present topic is controversial as Puzia et al. (2005) reported that up to one third of the GCs in a sample of seven early-type galaxies could have intermediate, spectroscopic ages in the range 5 – 10 Gyr.

Actually, despite the observational efforts of the last years, the current topic still lacks from a well-defined, high-quality, representative sample of GCs in all types of galaxies. With GC systems roughly following a *universal*, gaussian-like, luminosity function that peaks at  $M_V \sim -7.5$  (e.g. Harris 2001), the use of 8 - 10 m class telescopes for spectroscopic studies of GC systems in galaxies beyond the Local Group is strongly demanded. Even so, with the available instrumentation, only a subsample of a few tenths –out of the brightest (say  $B \leq 23$ ) GCs– in a single galaxy are subject to be reasonably observed for stellar population diagnostics in, typically, 1–2 observing nights. As a consequence, the problem of age-dating GC subpopulations is still far from being addressed with the accuracy needed to derive conclusive results, specially if we take into account that our current knowledge is still biased to a few –the brightest– GCs in a few –the closest– galaxies. It is therefore clear that larger samples of GCs in much larger samples of galaxies over a wide variety of types are necessary to face, from a more robust, statistical point of view, the problem of GC formation in the Universe.

The present paper on the GC system of NGC 1407 is just intended to be a step forward in the, presumably, long process of understanding the stellar populations of extragalactic GCs, and their conclusions do not necessarily have to be generalized to other galaxies. With an absolute magnitude in  $K$ –band of  $M_K \sim -25.6$  (Jarrett et al. 2000), NGC 1407 is a massive E0 dominating the Eridanus region of galaxies (e.g. Trentham et al. 2006; Brough et al. 2006) that may be the progenitor of a brightest cluster galaxy (BCG). Its current location at the centre of the group potential well, and intra-group medium (O’Sullivan et al. 2001), may give rise to a different evolutionary history than other group/cluster ellipticals. Indeed recent simulations of BCGs (de Lucia et al. 2006) suggests an unique hierarchical assembly history, with half of the final mass being added after redshifts of  $z \sim 0.5$  (i.e. the last 5 Gyrs). If this recent assembly has been dissipational (i.e. involved gas) then we might expect to find some signatures in the properties of the GC system.

In this paper we present unprecedented, high-quality spectroscopic data for a subsample of GCs in NGC1407. Section 2 is devoted to the GC sample selection, observations and data reduction. An analysis of the kinematics of the GC subsample is presented in Section 3. Section 4 describes the measurement of Lick/IDS, line-strength indices (Gorgas et al 1993; Worthey et al. 1994, hereafter W94; Worthey & Ottaviani 1997, hereafter W97), the ones are employed in Section 5 to determine ages, metallicities and abundance ratios of  $\alpha$ -elements for the galaxy and the GC spectra using different approaches. A qualitative description of the behavior of C and N sensitive Lick indices in our GC sample is presented in Section 6. Section 7 is reserved to discuss the most relevant results obtained in the previous sections, and a general overview of the paper is finally given in Section 8.

## 2. Sample selection, observations and data reduction

### 2.1. GC sample selection

GC candidates of NGC 1407 were selected on the basis of photometric data taken in the F435W and F814LP filters using the Advanced Camera for Surveys (ACS) in Wide Field Channel mode (WFC) on the *Hubble Space Telescope* (HST; proposal ID = 9427). We refer the reader to the papers by Harris et al. (2006) and Forbes et al. (2006; hereafter F06) for a thorough analysis of the above data.

Figure 1 illustrates the  $B$  versus  $B - I$ , color-magnitude diagram (CMD) of the GCs candidates on the basis of the photometric data given by F06 (left panel), as well as the corresponding ACS/WFC imaging of NGC 1407 in the F814LP filter (right panel). As expected for a massive E galaxy, the GC system of NGC 1407 exhibits a clear bimodality in its color distribution, with red and blue subpopulations peaking at  $B - I \sim 1.61$  and 2.06 respectively (F06). Nevertheless, as discussed in Harris et al., the high-luminosity regime ( $B \lesssim 23.5$ ) of this CMD does not exhibit an obviously bimodal distribution. There exists a clear tilt in the color-magnitude relation of the blue GC subpopulation that makes the high-luminosity, blue GCs occupy the position of the bright end of the red GC peak. Such a phenomenon, first reported by Ostrov et al. (1998) for the GC system of NGC 1399 in Fornax (see also Dirsch et al. 2003), has been detected for M87 and NGC 4649 in Virgo (Strader et al. 2006) and seems to be commonplace for bright Es dominating the central regions of groups or clusters of galaxies (Harris et al.). A mass-metallicity relationship, presumably though self-enrichment, has been proposed in the above papers as a plausible explanation for this phenomenon. Spectroscopic metallicities will help to test this proposal.

From the high-luminosity regime of the CMD in Fig. 1, 21 GC candidates spanning a

wide color range were selected for spectroscopic purposes (circled points). It is worth noting that, as discussed by Harris et al., some of the luminous objects we observed could be remnant nuclei of disrupted, accreted dEs, although our subsequent analysis finds no particular properties supporting the above hypothesis. Because of the tilt of the blue sequence, the separation between blue and red GC subpopulations is not well defined. Throughout this paper, we have considered a tentative division at  $B - I = 1.87$  when it has been necessary. Basic parameters of the selected GC candidates, such as coordinates, colors, magnitudes and heliocentric radial velocities are listed in Table 1.

## 2.2. Observations and data reduction

Spectroscopic data for 21 GC candidates in NGC 1407 were obtained on 2003 October 21 – 23 at the Keck I telescope using the Low-Resolution Imaging Spectrometer (LRIS; Oke et al. 1995) in multi-object mode. With seeing varying from 0.6 to 0.8 arcsec over the three nights, all the exposures were made through a slitmask with 0.8 arcsec width slits of  $\sim 8$  arcsec typical length. The total exposure time for the GC candidates was 7 hours ( $14 \times 30$  min exposures). In addition, a 15 min ( $3 \times 5$  min) spectrum of NGC 1407 was obtained through a 0.8 arcsec width long-slit positioned along the major axis of the galaxy (P.A. =  $56^\circ$ ; Longo et al. 1994, although note that it is not particularly well defined for an E0 galaxy). In order to transform our data to the Lick/IDS spectro-photometric system, a subsample of five K – G giant stars (HR 2002, HR 2153, HR 2459, HR 7429 and HR 8165) from the Lick/IDS stellar library (W94; W97) were also observed through the long-slit mask during twilights. Short exposure times of  $\sim 1$  sec were required to avoid saturation in their spectra. In turn, three spectro-photometric standard stars from Oke (1990) were observed at different air masses for calibrating purposes.

Making use of LRIS-B together with a dichroic splitting at  $6800\text{ \AA}$ , spectra in the ranges  $\sim 3400 - 5800\text{ \AA}$  (blue) and  $\sim 7100 - 9100\text{ \AA}$  (red) were simultaneously obtained for both the GCs<sup>1</sup> and the galaxy. On the blue side, a 600 line  $\text{mm}^{-1}$  grism blazed at  $4000\text{ \AA}$  provided a reciprocal dispersion of  $0.6\text{ \AA pix}^{-1}$  and an overall spectral resolution (full width at half maximum; FWHM) of  $3.7\text{ \AA}$ . The analysis of the red side data is deferred to a forthcoming paper.

For each of the 14 GC mask frames, bi-dimensional (2D) distortions were mapped by fitting polynomials to the edges of the individual slitmasks. The raw mask frames, as well

---

<sup>1</sup>Shifts in the GC spectral ranges of up to  $\sim \pm 300\text{ \AA}$  with respect to the above mean values were obtained because of the location of the different slitmasks along the dispersion direction within the mask

as their corresponding overheads (flatfield and arc frames), were straightened by using the derived polynomials, thus allowing the different slitmask regions in each mask frame to be properly extracted into a single, rectangular frame. After this, a standard spectroscopic reduction procedure (bias subtraction, flatfielding, cosmic ray cleaning, C-distortion correction, wavelength calibration, S-distortion, sky subtraction, extinction correction, flux calibration, and final spectrum extraction) was performed for each single slitmask with  $\text{RED}_{\text{M}}^{\text{UC}}\text{E}^2$  (Cardiel 1999), as well as for the long-slit spectra of the galaxy and the calibrating stars. The major improvement of this reduction package is that it allows a parallel treatment of data and error frames along the reduction procedure, thus producing an associated, reliable error spectrum for each individual data spectrum.

In order to optimize the total exposure time of our targets, wavelength calibrating arcs were only taken right after one of the various GC mask exposures in each night. Because of flexures, small shifts in both spatial and spectral directions were measured among different GC mask frames. While spatial flexures did not remain a problem after flatfielding and extracting the slitmask regions into single frames, the existence of spectral zero-point shifts among GC mask frames could in principle prevent a proper wavelength calibration for all the GC mask frames. In order to avoid this, for each slitmask of frames without its own arc, spectral offsets with respect to the reference slitmask were measured by cross-correlating their spectra around the bright O I skyline at  $\sim 5577\text{\AA}$ . After correcting the slitmask zero-points, a standard wavelength calibration for all the GC mask frames could finally be performed on the basis of the available arcs.

The overall sky and galaxy background level in each GC mask frame was computed by means of a standard, linear interpolation along the spatial direction of the signal measured at regions free from the contamination with the object of interest. Special care was taken for the shortest GC slitlets –of just  $\sim 4 - 5$  arcsec– as only a few pixels near the edges of the slits could be safely used for this purpose. Moreover, GC mask frames #06 and #13 exhibited a rapidly changing galaxy background since they were located in close proximity to the galaxy. In these two cases, rather than linear fits, higher order ( $\leq 3$ ) polynomial fits to the background levels were performed.

### 3. Radial velocity measurements and GC kinematics

Radial velocities for the GC candidates were derived using the MOVEL algorithm described in González (1993), which is an improvement of the classic Fourier quotient method

---

<sup>2</sup><http://www.ucm.es/info/Astrof/software/reduceme/reduceme.html>

Table 1: Basic data for GC candidates in NGC 1407

Slit ID	RA(J2000)	DEC(J2000)	<i>B</i> (mag)	<i>B</i> – <i>I</i> (mag)	RV (km s <sup>–1</sup> ) <sup>a</sup>
#01	03:40:09.42	–18:33:37.4	20.98 ± 0.02	1.82 ± 0.03	1196 ± 2(23)
#03	03:40:11.60	–18:35:13.1	21.83 ± 0.02	1.93 ± 0.03	2204 ± 4(29)
#04	03:40:18.14	–18:33:10.3	21.81 ± 0.02	1.86 ± 0.03	1717 ± 3(19)
#05	03:40:14.74	–18:33:52.6	22.06 ± 0.02	1.88 ± 0.03	1669 ± 3(20)
#06	03:40:11.00	–18:35:55.5	21.83 ± 0.02	1.79 ± 0.03	1379 ± 3(25)
#07	03:40:17.56	–18:33:59.6	22.16 ± 0.02	1.91 ± 0.03	2055 ± 4(18)
#08	03:40:12.69	–18:34:23.0	22.12 ± 0.02	1.70 ± 0.03	1843 ± 5(23)
#09	03:40:17.16	–18:33:23.4	22.08 ± 0.02	1.53 ± 0.03	1642 ± 8(26)
#11	03:40:09.38	–18:34:46.0	22.31 ± 0.02	1.91 ± 0.03	1652 ± 6(30)
#12	03:40:09.16	–18:34:59.2	22.35 ± 0.02	2.05 ± 0.03	2254 ± 5(22)
#13	03:40:10.06	–18:35:53.2	22.36 ± 0.02	1.76 ± 0.03	1558 ± 6(26)
#14	03:40:14.90	–18:35:11.9	22.30 ± 0.02	2.04 ± 0.03	1947 ± 4(21)
#15	03:40:09.43	–18:34:10.4	22.38 ± 0.02	1.90 ± 0.03	1636 ± 4(19)
#17	03:40:14.61	–18:32:29.2	22.43 ± 0.02	2.03 ± 0.03	1920 ± 3(22)
#18	03:40:12.55	–18:34:10.6	22.43 ± 0.02	2.00 ± 0.03	2402 ± 11(23)
#22	03:40:14.04	–18:34:01.6	22.58 ± 0.02	2.07 ± 0.04	1547 ± 3(17)
#26	03:40:15.25	–18:32:11.5	22.36 ± 0.02	1.65 ± 0.03	1907 ± 6(30)
#27	03:40:17.64	–18:33:35.9	22.75 ± 0.02	2.08 ± 0.03	1839 ± 5(26)
#30	03:40:10.28	–18:34:42.8	22.56 ± 0.02	2.02 ± 0.04	1287 ± 7(34)
#31	03:40:13.76	–18:35:05.3	22.76 ± 0.02	2.08 ± 0.03	62 ± 4(21)
#33	03:40:15.85	–18:34:06.9	22.74 ± 0.02	1.74 ± 0.03	1732 ± 9(22)

<sup>a</sup>Final heliocentric radial velocities of the GC candidates together with their random and absolute errors (in parentheses; see text). Candidate #31 was found to be a foreground Galactic star.

by Sargent et al. (1977) to determine RVs and velocity dispersions of galaxy spectra. Although the spectral resolution of our data does not allow us to measure reliable velocity dispersions for the GCs, we preferred to use this method given that, from previous experience, we know it provides a more robust RV determination than classical cross-correlation procedures. In order to prevent uncertainties in the method that appear when velocity dispersion solutions are very close to zero, the GC spectra were broadened by convolving them with a Gaussian function of  $\sigma = 50 \text{ km s}^{-1}$ .

The five Lick/IDS stars observed during the run were separately used as reference spectra for this method, thus deriving five independent values of RVs for each GC. In each case, random errors in the derived RVs were computed by MonteCarlo simulations in which Gaus-

sian noise is added to the object and reference spectra according to their corresponding error spectra. Final values for radial velocities were computed as error-weighted means of the five individual estimations, with the larger of either the typical error of the error-weighted mean or the error-weighted standard deviation of the single determinations being considered as the final random error. It is important to note that such final random errors do not account for any systematic effect arising, for example, from uncertainties in the wavelength calibration. In other words, the derived RVs and their errors are fully consistent within their own system, but small offsets could still be affecting the true values of the radial velocities. In order to account for errors due to small deviations from a linear wavelength scale, the GC spectra were also cross-correlated with an appropriate *MILES*<sup>3</sup> (Sánchez-Blázquez et al. 2006a; Cenarro et al. 2007) template in  $\sim 150$  small, overlapping spectral regions along wavelength. The *rms* standard deviation of all the RV solutions obtained from each individual region can be considered as a more reliable estimation of the absolute uncertainties of the RVs. The final heliocentric radial velocities of the GC candidates, their corresponding random errors and their absolute errors (within parenthesis) are listed in last column of Table 1. Candidate #31 turned out to be a foreground Galactic star that was rejected from further analysis in this paper.

The above procedure was followed to measure the kinematics of the integrated central spectrum of NGC 1407 ( $R_{\text{eff}}/8$  aperture). An  $R_{\text{eff}}$  of 36.4 arcsec for NGC 1407 was taken from Diehl & Statler (2006). The derived central velocity dispersion and the heliocentric radial velocity are  $293.5 \pm 4.1 \text{ km s}^{-1}$  and  $1785.6 \pm 5.2 \text{ km s}^{-1}$  respectively. These values are in reasonably good agreement with previous determinations as given in Hyperleda, i.e.  $273 \text{ km s}^{-1}$  and  $1783 \pm 26 \text{ km s}^{-1}$  respectively.

On the basis of the 20 bona fide GCs, the mean heliocentric radial velocity of our GC subsystem ( $RV_{\text{sys}}$ ) is  $1769 \pm 70 \text{ km s}^{-1}$ , with an overall *rms* standard deviation of  $313 \text{ km s}^{-1}$ . Figure 3 displays the distribution of such GC RVs as a function of the projected distance from the center of NGC 1407 (galactocentric radius;  $R_{\text{gc}}$ ). A distance of 20.9 Mpc to NGC 1407 (F06) has been assumed for this figure (note that the galaxy could be as far as 28.8 Mpc; Tonry et al. 2001). In any case, it is clear that the dispersion of the GC RVs seems to decrease with the increasing projected distance. In particular, when the *rms* standard deviation of the GC RVs is separately computed within three different radial bins, we obtain the following values:  $361 \text{ km s}^{-1}$  ( $R_{\text{gc}} < 10 \text{ kpc}$ ),  $244 \text{ km s}^{-1}$  ( $5 < R_{\text{gc}} < 15 \text{ kpc}$ ) and  $149 \text{ km s}^{-1}$  ( $R_{\text{gc}} > 10 \text{ kpc}$ ). This behaviour could have important implications for orbital properties of the GCs within the potential well of the galaxy. Although our GC sample is not large

---

<sup>3</sup>Medium resolution INT Library of Empirical Spectra; <http://www.ucm.es/info/Astrof/miles/miles.html>

enough to make definitive statements on this issue, the existence of radial orbits (rather than isotropic ones) would help to explain the distribution of GC RVs shown in Fig. 3. A more detailed analysis on the GC orbits, galaxy mass and dark matter content estimates are deferred to a forthcoming paper.

Rotation around the host galaxy is a common signature of GC systems, although there exists no well-established pattern for massive Es. Whilst some GC systems do not exhibit any rotation (NGC 1399; Richtler et al. 2004), others show significant rotation (M87, Côté et al. 2001; NGC 4472, Zepf et al. 2000; Côté et al. 2003). In Figure 4 we illustrate the GC radial velocities relative to  $RV_{\text{sys}}$  as a function of the projected distance to four different directions: the major and minor axes, and the two intermediate orientations. It is clear from the figure that there exist no obvious rotation around any direction. There may still be a weak rotating signature for MP GCs although, once again, the small number of GCs does not allow us to carry out a reliable statistical analysis.

#### 4. Measurement of Lick indices

The Lick/IDS system of line-strength indices (Gorgas et al. 1993; W94) has been widely used as the reference system to interpret the stellar population properties in the optical spectral range of a large variety of stellar systems (see e.g. Trager et al. 2000a,b; Sánchez-Blázquez et al. 2006b and references therein). It is worth mentioning though that, during the past few years, there have been significant efforts in developing much improved empirical stellar libraries (e.g. the Indo-US stellar library, Valdés et al. 2004; *MILES*, Sánchez-Blázquez et al. 2006a, Cenarro et al. 2007) that comprise larger samples of stars, over wider ranges of atmospheric parameters and with a higher spectral resolution than the Lick stellar sample. In the near future, these works are expected to constitute the new reference system for forthcoming studies on this topic. SSP model predictions on the basis of such libraries (e.g. Vazdekis et al. 2007, in preparation) are expected to overcome some limitations of the current ones based on the Lick stellar library.

Table 2. List of Lick/IDS indices measured in this work.

$I^a$	$\sigma$ (km s $^{-1}$ ) <sup>b</sup>	$\Delta I^c$	Errors		$t$ -tests	
			$\sigma_{\text{typ}}^d$	$\sigma_{\text{rms}}^d$	$t_{\text{typ}}^f$	$t_{\text{rms}}^g$
$H\delta_A(\text{\AA})$	325	-0.075	0.070	0.097	1.1	0.8
$H\delta_F(\text{\AA})$	325	-0.020	0.058	0.052	0.4	0.4
$CN_1(\text{mag})$	325	-0.011	0.002	0.002	5.3	5.2
$CN_2(\text{mag})$	325	-0.016	0.002	0.005	6.8	3.6
$Ca4227(\text{\AA})$	300	+0.034	0.028	0.035	1.2	1.0
$G4300(\text{\AA})$	300	-0.053	0.052	0.112	1.0	0.5
$H\gamma_A(\text{\AA})$	275	-0.528	0.042	0.031	12.7	17.2
$H\gamma_F(\text{\AA})$	275	-0.233	0.033	0.033	7.0	7.0
$Fe4383(\text{\AA})$	250	-0.181	0.076	0.031	2.4	5.9
$Ca4455(\text{\AA})$	250	-0.302	0.072	0.059	4.2	5.1
$Fe4531(\text{\AA})$	250	-0.377	0.073	0.054	5.2	6.9
$Fe4668(\text{\AA})$	250	+0.357	0.077	0.040	4.6	9.0
$H\beta(\text{\AA})$	225	+0.053	0.025	0.012	2.1	4.3
$Fe5015(\text{\AA})$	200	-0.022	0.052	0.061	0.4	0.4
$Mg_1(\text{mag})$	200	-0.004	0.001	0.002	5.9	1.6
$Mg_2(\text{mag})$	200	-0.010	0.001	0.002	11.5	4.7
$Mgb(\text{\AA})$	200	+0.074	0.027	0.022	2.8	3.4
$Fe5270(\text{\AA})$	200	+0.210	0.030	0.018	7.0	11.5
$Fe5335(\text{\AA})$	200	+0.223	0.029	0.039	7.8	5.7
$Fe5406(\text{\AA})$	200	+0.087	0.030	0.041	2.9	2.1

Note. — (a) Lick index; (b) Overall spectral resolution at which the index was measured; (c) Error-weighted, index offset between the spectro-photometric system of this work ( $TW$ ) and the corresponding Lick system (W94; W97):  $\Delta I = I(TW) - I(W94/W97)$ ; (d) Typical error of the offset  $\Delta I$ ; (e) Error-weighted, *rms*, residual standard deviation of the offset

$\Delta I$ ; (f, g) Values of  $t$ -tests using  $\sigma_{\text{typ}}$  and  $\sigma_{\text{rms}}$  as estimates of the offset uncertainties respectively. Assuming a significance level of  $\alpha = 0.1$  and 4 (5 – 1) degrees of freedom, the critical value for the bilateral test is  $t_{\alpha/2, 4} = 2.132$ .

We have measured all the Lick indices within the spectral range of the GCs and the galaxy spectra. In order to compare our index measurements with those predicted by SSPs models in the Lick system, we matched both the spectral resolution and the spectro-photometric system of the models. Since the spectral resolution of the Lick stellar library varies with wavelength, each single index had to be measured at a given spectral resolution that, in all cases, was much lower than the overall spectral resolution of the GC spectra ( $\sim 100 \text{ km s}^{-1}$ ). Hence, before measuring the indices, all the GC spectra were broadened by convolving with an appropriate Gaussian function to match the required spectral resolution. For the galaxy spectrum, with an overall spectral resolution  $\sim 300 \text{ km s}^{-1}$ , we applied the sigma-dependent, polynomial corrections given in Gorgas et al. (2007; submitted).

As mentioned in Section 2.2, the 5 stars in common with the Lick stellar library were employed to correct our data to the Lick spectro-photometric system. After broadening their spectra to match the required spectral resolutions, the Lick indices of the stars were measured and compared with those published in W94 and W97, as it is illustrated in Figure 8.3. For each index, an error-weighted, mean offset was derived with respect to the Lick system. The index errors estimated in W94 and W97 for a typical, single-observation, star were assumed for HR 2153, HR 2459, and HR 8165 (filled circles). For the *standards* HR 2002 and HR 7429 (open squares), with 41 and 64 repeated observations respectively, their corresponding typical errors were instead considered.

Even though all the derived offsets were systematically applied to our data, we computed *t*-tests to check whether the derived calibrations were statistically significant or not. For a significance level of  $\alpha = 0.1$  and 4 degrees of freedom (5 data points minus 1 for the mean), the derived offsets can be considered statistically significant if their corresponding *t*-tests are larger than  $\sim 2.1$ . Note that although the above calibrations rely on an error-weighted *effective* number of stars in the range 1.6 – 3.0 (depending on the index), the derived offsets seem to be reasonably well constrained. In fact, the two Lick *standard* stars –that essentially dominate the calibrations because of their considerably smaller errors– exhibit an excellent agreement in nearly all cases. The only possible exception is G4300 which appears slightly less well constrained.

The Lick indices we have measured are listed in Table 2, together with the spectral resolutions at which the indices were measured, the derived offsets w.r.t the Lick system, their errors and their corresponding *t*-tests. To prevent possible underestimates of the offset uncertainties arising from the small number of points, we computed not only the typical error of the offsets ( $\sigma_{\text{typ}}$ ) but also the error-weighted, *rms*, residual standard deviation of the offsets ( $\sigma_{\text{rms}}$ ). Consequently, the *t*-test values are provided for both error estimates ( $t_{\text{typ}}$  and  $t_{\text{rms}}$ ).

In addition to the above Lick indices, we have also computed the indices

$$[\text{MgFe}]' = \sqrt{\text{Mgb} \times (0.72 \times \text{Fe5270} + 0.28 \times \text{Fe5335})}, \quad (1)$$

as defined by Thomas et al. (2003a; hereafter TMB03), and

$$\langle \text{Fe} \rangle = (\text{Fe5270} + \text{Fe5335})/2. \quad (2)$$

In Table 3 we present the final index measurements for the GCs and the central galaxy spectrum.

Table 3. Lick indices of the GCs and the  $R_{\text{eff}}/8$  central spectrum of NGC 1407.

Slit ID	$S/N$ ( $\text{Å}^{-1}$ )	$\text{H}\delta_A$ ( $\text{\AA}$ )	$\text{H}\delta_F$ ( $\text{\AA}$ )	$\text{CN}_1$ (mag)	$\text{CN}_2$ (mag)	$\text{Ca42}$ ( $\text{\AA}$ )	$\text{G43}$ ( $\text{\AA}$ )	$\text{H}\gamma_A$ ( $\text{\AA}$ )	$\text{H}\gamma_F$ ( $\text{\AA}$ )	$\text{Fe43}$ ( $\text{\AA}$ )	$\text{Ca44}$ ( $\text{\AA}$ )	$\text{Fe45}$ ( $\text{\AA}$ )	$\text{Fe46}$ ( $\text{\AA}$ )	$\text{H}\beta$ ( $\text{\AA}$ )	$\text{Fe50}$ ( $\text{\AA}$ )	$\text{Mg}_1$ (mag)	$\text{Mg}_2$ (mag)	$\text{Mgb}$ ( $\text{\AA}$ )	$\text{Fe52}$ ( $\text{\AA}$ )	$\text{Fe53}$ ( $\text{\AA}$ )	$\text{Fe54}$ ( $\text{\AA}$ )	[MgFe]'	$\langle \text{Fe} \rangle$ ( $\text{\AA}$ )
#01	56 – 93	1.06	1.60	0.007	0.047	0.48	3.94	-2.33	0.54	3.05	1.21	2.41	1.00	2.08	3.74	0.050	0.142	2.28	1.47	1.24	0.85	1.79	1.35
		0.13	0.09	0.004	0.004	0.07	0.12	0.13	0.08	0.17	0.09	0.13	0.19	0.08	0.17	0.002	0.002	0.09	0.10	0.11	0.08	0.06	0.07
#03	20 – 35	-1.28	0.59	0.131	0.175	0.68	5.10	-4.11	-0.57	3.91	1.59	3.78	2.07	1.42	4.30	0.075	0.208	3.52	1.57	1.67	1.40	2.37	1.62
		0.39	0.27	0.011	0.013	0.19	0.31	0.36	0.22	0.44	0.23	0.34	0.51	0.21	0.44	0.005	0.006	0.22	0.25	0.28	0.21	0.17	0.19
#04	31 – 53	-0.01	0.92	0.022	0.054	0.54	4.35	-2.83	0.11	2.81	1.43	2.61	1.89	1.92	3.77	0.051	0.155	2.48	1.53	1.42	0.83	1.93	1.47
		0.25	0.17	0.007	0.008	0.12	0.21	0.23	0.14	0.30	0.16	0.23	0.34	0.14	0.29	0.003	0.004	0.15	0.17	0.19	0.14	0.10	0.13
#05	22 – 41	0.75	1.50	0.068	0.124	0.32	4.11	-2.74	0.18	3.64	1.62	3.77	-0.37	1.84	5.15	0.070	0.205	3.05	2.07	1.58	1.47	2.43	1.83
		0.35	0.24	0.010	0.011	0.17	0.28	0.30	0.18	0.39	0.21	0.30	0.46	0.18	0.38	0.004	0.005	0.20	0.22	0.24	0.18	0.13	0.16
#06	28 – 49	1.35	1.74	0.021	0.069	0.64	3.78	-1.45	0.74	2.37	0.82	3.69	1.45	1.93	3.67	0.035	0.126	2.00	1.69	1.35	0.74	1.79	1.52
		0.26	0.18	0.007	0.009	0.13	0.22	0.24	0.15	0.33	0.17	0.24	0.37	0.15	0.31	0.003	0.004	0.16	0.18	0.21	0.16	0.11	0.14
#07	21 – 37	-0.02	1.26	0.076	0.101	0.74	4.23	-2.30	0.80	3.47	1.28	2.05	0.25	1.89	4.69	0.066	0.176	2.93	2.20	1.85	1.43	2.48	2.03
		0.37	0.25	0.010	0.012	0.18	0.30	0.33	0.20	0.43	0.23	0.33	0.50	0.19	0.41	0.005	0.006	0.22	0.23	0.26	0.20	0.14	0.18
#08	18 – 25	1.53	1.56	0.012	0.028	0.64	3.54	-1.03	1.25	2.20	0.57	2.19	0.90	2.29	4.27	0.033	0.107	1.85	0.93	1.14	1.13	1.35	1.03
		0.43	0.30	0.012	0.015	0.22	0.38	0.42	0.26	0.59	0.31	0.47	0.69	0.28	0.60	0.007	0.008	0.30	0.36	0.41	0.30	0.22	0.27
#09	26 – 37	2.86	2.42	-0.048	-0.012	0.22	2.63	0.99	2.03	0.53	0.80	2.00	-1.06	2.43	1.73	0.015	0.068	0.48	1.12	0.96	0.22	0.72	1.04
		0.28	0.19	0.008	0.010	0.15	0.27	0.27	0.17	0.41	0.20	0.31	0.48	0.19	0.42	0.004	0.005	0.22	0.23	0.27	0.21	0.17	0.18
#11	14 – 25	-1.41	0.43	0.099	0.136	0.91	5.14	-3.71	-0.58	3.65	1.97	3.70	1.57	1.51	5.25	0.060	0.177	2.78	2.02	1.52	1.25	2.29	1.77
		0.56	0.38	0.015	0.018	0.26	0.44	0.50	0.31	0.63	0.32	0.48	0.74	0.29	0.62	0.007	0.008	0.32	0.35	0.41	0.30	0.22	0.27
#12	13 – 25	-2.11	0.27	0.139	0.182	0.39	4.79	-5.25	-1.09	4.55	1.20	3.58	1.92	1.63	4.53	0.091	0.258	4.17	2.65	2.45	1.22	3.29	2.55
		0.61	0.40	0.016	0.019	0.28	0.46	0.52	0.31	0.62	0.34	0.47	0.72	0.29	0.62	0.007	0.009	0.32	0.35	0.38	0.30	0.21	0.26
#13	17 – 31	1.57	1.14	-0.006	0.041	0.30	3.87	-1.95	0.96	3.37	1.34	2.32	1.26	2.02	1.72	0.035	0.144	2.30	1.44	1.51	1.02	1.83	1.48
		0.43	0.31	0.012	0.014	0.21	0.36	0.39	0.23	0.50	0.26	0.40	0.59	0.23	0.51	0.005	0.007	0.26	0.28	0.32	0.24	0.17	0.22
#14	17 – 33	-1.48	0.68	0.116	0.162	1.06	5.80	-5.81	-0.51	5.03	1.66	3.37	2.98	1.43	3.12	0.081	0.228	4.30	2.01	2.13	1.31	2.96	2.07
		0.48	0.32	0.013	0.015	0.21	0.35	0.41	0.23	0.47	0.26	0.38	0.55	0.22	0.49	0.005	0.007	0.24	0.27	0.29	0.22	0.17	0.20
#15	16 – 30	-1.05	0.84	0.075	0.105	0.78	5.50	-3.55	0.19	3.46	1.71	3.51	4.05	1.68	4.28	0.074	0.197	3.54	1.53	1.83	0.66	2.39	1.68
		0.48	0.32	0.013	0.015	0.22	0.36	0.41	0.25	0.52	0.27	0.40	0.58	0.24	0.52	0.006	0.007	0.26	0.29	0.33	0.26	0.19	0.22
#17	18 – 37	-1.45	0.56	0.136	0.194	0.80	5.27	-4.93	-0.98	4.05	1.38	3.35	3.10	2.19	5.96	0.102	0.257	4.12	2.11	1.87	1.28	2.90	1.99
		0.44	0.29	0.012	0.014	0.20	0.33	0.38	0.23	0.46	0.24	0.34	0.49	0.20	0.42	0.005	0.006	0.22	0.24	0.27	0.20	0.16	0.18
#18	14 – 26	-0.99	0.09	0.076	0.105	0.79	4.64	-4.08	-0.89	3.12	1.81	3.75	1.41	2.06	3.85	0.076	0.214	3.25	2.00	2.21	1.47	2.59	2.11
		0.56	0.38	0.015	0.018	0.26	0.44	0.50	0.31	0.65	0.33	0.47	0.73	0.29	0.63	0.007	0.008	0.32	0.35	0.39	0.29	0.21	0.26
#22	12 – 26	-2.88	-0.29	0.191	0.229	1.24	4.53	-4.98	-1.00	4.66	1.66	3.77	2.91	1.42	3.58	0.121	0.273	4.44	2.53	2.73	1.69	3.39	2.63
		0.68	0.45	0.019	0.022	0.29	0.49	0.54	0.32	0.64	0.35	0.48	0.70	0.29	0.62	0.007	0.009	0.31	0.33	0.37	0.28	0.21	0.25
#26	22 – 34	2.41	2.14	-0.034	-0.003	0.59	3.43	-1.08	1.02	2.59	1.01	2.33	0.00	2.26	2.88	0.039	0.116	1.57	0.96	0.78	0.62	1.19	0.87
		0.34	0.24	0.010	0.012	0.18	0.31	0.33	0.20	0.45	0.23	0.35	0.53	0.21	0.46	0.005	0.006	0.24	0.27	0.31	0.23	0.17	0.20
#27	11 – 25	-2.65	0.90	0.160	0.209	1.07	5.33	-5.85	-1.18	4.76	1.49	2.64	5.44	1.39	4.96	0.102	0.281	4.83	2.49	1.65	1.78	3.30	2.07
		0.73	0.46	0.020	0.023	0.31	0.52	0.59	0.34	0.68	0.37	0.54	0.72	0.31	0.65	0.007	0.009	0.33	0.36	0.40	0.30	0.23	0.27
#30	8 – 14	-0.72	0.92	0.065	0.120	1.20	3.60	-2.99	-0.52	3.46	1.15	4.02	2.37	1.34	3.33	0.049	0.227	4.12	2.08	1.73	1.67	2.86	1.90
		1.02	0.70	0.028	0.033	0.45	0.83	0.88	0.55	1.12	0.61	0.81	1.25	0.51	1.13	0.012	0.015	0.52	0.60	0.69	0.52	0.39	0.46
#33	11 – 19	3.90	2.38	-0.071	-0.023	1.34	1.69	0.56	1.75	2.53	1.44	3.07	2.61	2.57	2.90	0.052	0.121	2.09	1.39	1.16	1.05	1.67	1.28
		0.65	0.47	0.019	0.023	0.33	0.62	0.61	0.38	0.84	0.44	0.65	0.95	0.38	0.85	0.009	0.011	0.43	0.48	0.54	0.40	0.29	0.36
$R_{\text{eff}}/8$	164 – 281	-3.17	-0.17	0.161	0.207	1.28	5.45	-6.46	-1.92	5.45	2.14	3.98	8.17	1.52	6.18	0.180	0.355	5.31	3.01	2.71	1.85	3.94	2.86
		0.06	0.10	0.001	0.004	0.04	0.09	0.05	0.04	0.13	0.20	0.09	0.09	0.05	0.20	0.001	0.001	0.05	0.04	0.11	0.07	0.03	0.06

 Note. — Index errors accounting for photon statistic and uncertainties in RVs are given below the index measurements. The indices  $\langle \text{Fe} \rangle$  and [MgFe]' are also included in the table.

<sup>a</sup>Mean signal-to-noise ratios per angstrom of the final spectra at the location of the bluest and reddest indices,  $\text{H}\delta_A$  and  $\text{Fe5406}$ .

## 5. Ages, metallicities and $\alpha$ -element abundance ratios for the GCs

In this section we study the stellar population properties of the GCs. For this purpose, we make use of the Lick index measurements presented in the previous section along with independent approaches to derive ages, metallicities and  $\alpha$ -element abundance ratios. In Section 5.1, a first estimate of the GC metallicities is obtained on the basis of the metallicity calibration by Strader & Brodie (2004). The other two approaches (Section 5.2) rely on the SSP models of TMB03 and Thomas et al. (2004; hereafter TMK04), which account for three different  $[\alpha/\text{Fe}]$  ratios as well as for blue horizontal branch (BHB) effects for metallicities  $\leq -0.5$  dex (Maraston et al. 2003). Ages, metallicities and  $[\alpha/\text{Fe}]$  ratios derived for the GCs and the central spectrum of NGC 1407 according to these different procedures are presented in Table 4 and compared in Section 5.3.

### 5.1. PCA metallicities

One of the simplest approaches to estimate the metallicities of GCs is the use of empirical metallicity calibrators, that is, photometric and/or spectroscopic indicators which are sensitive to metallicity effects and whose behaviors are well calibrated on the basis of GGCs (Zinn & West 1984; Armandroff & Zinn 1988; Brodie & Huchra 1991; Carretta & Gratton 1997; Kraft & Ivans 2003). Certainly, the major advantage of using metallicity calibrators is that the derived metallicities are model independent. However, one has to deal with the fact that the ages, abundance ratios and/or the metallicity range of the GCs under study may not be the same as those in GGCs. However, given that the existence of young ( $\lesssim 5$  Gyr) GCs does not seem to be commonplace in the GC systems of E galaxies (e.g. Strader et al. 2005), using metallicity calibrators on extragalactic GCs is a reasonable starting point.

We have made use of the metallicity calibration by Strader & Brodie (2004), which is based on a principal component analysis (PCA) of 11 Lick indices for a sample of 39 GGCs. The first principal component (PC1) is responsible for 94% of the total variance, with all the 11 indices having similar relative contributions. The fact that the Balmer indices show opposite signs to the metal indices suggests that PC1 is indeed correlated with the GGC metallicity. The metallicity values ( $[\text{m}/\text{H}]$ ) derived from PC1 for our 20 GCs are listed in the second column of Table 4, with uncertainties resulting from the standard propagation of errors. As noted in Strader & Brodie, it is worth mentioning that  $[\text{m}/\text{H}]$ , although being presumably close to the Zinn & West (1984) metallicity scale, may not strictly reflect neither  $[\text{Fe}/\text{H}]$  nor overall metallicity ( $[\text{Z}/\text{H}]$ ). In this sense, a word of caution is reasonable before any comparison with the results derived from other techniques. We refer the reader to Strader & Brodie (2004) for a more detailed discussion on this topic.

Making use of the photometric data in F06 (see also Table 1), Figure 6 illustrates the corresponding color-metallicity relationship between the PCA metallicities and F06 photometry. The tight correlation existing between both parameters supports the idea that the color distribution of GC systems is mainly driven by metallicity. In agreement with previous work on GC systems of other giant Es, we find the red GC population to be very metal rich, with some GCs reaching  $[m/H]$  values above solar. At the high metallicity regime ( $[m/H] > -0.7$ ), the steepening of the color-metallicity relationship qualitatively resembles the one presented in Yoon, Yi & Lee (2006) although, as mentioned above, extrapolations beyond solar metallicity are not completely safe and it could be just an artifact of the fact that the PCA calibration relies on GGCs.

## 5.2. Ages, metallicities and abundance ratios from SSP models

### 5.2.1. Using a multivariate analysis

Metallicities ( $[Z/H]$ ), ages and  $[\alpha/Fe]$  ratios for the GCs and galaxy starlight were computed from their Lick indices by performing multivariate fits to the TMB03 and TMK04 SSP models. For comparisons, the same procedure was performed for a sample of 41 GGCs by Schiavon et al. (2005). The application of this technique to GCs is described in detail in Proctor et al. (2004). Briefly, 12–18 indices were fit simultaneously for  $[Z/H]$ , age and  $[\alpha/Fe]$  to the grid of models until  $\chi^2$  was minimized. Any indices which deviated from the fit were excluded and  $\chi^2$  recalculated (here, we employed three iterations with rejections of  $5\sigma$ – $3\sigma$ – $5\sigma$ ). It is important to keep in mind that this method makes use of all the available indices, so the *best* solution relies on much more information than if it had been derived from a single, index-index diagram. This advantage may turn into a problem because of the fact that the behavior of some elements (like, e.g. C, N and Ca) is not well understood and/or accounted for the models, so the inclusion of their corresponding indices –or indices affected to some extent by these elements– in the  $\chi^2$  procedure may affect the reliability of the final result. For this reason, several Lick indices were routinely rejected during this process: i) CN<sub>1</sub> and CN<sub>2</sub>; as it will be discussed later, these indices are extremely enhanced relative to the models; ii) Ca4227; it exhibits a large scatter around the models without any reasonable explanation. Actually, despite Ca is an alpha element like Mg, its behavior is not well understood yet (see Worthey 1992, Vazdekis et al. 1997, Trager et al. 1998, Saglia et al. 2002, Cenarro et al. 2003, Thomas et al. 2003b, Cenarro et al. 2004) and we preferred to exclude it from the present analysis; iii) Fe4531 and Fe5015; as they look systematically wrong –unlike other Fe indices– in the GGC comparison sample. Errors in the output parameters were computed by means of Montecarlo simulations according to the individual errors of all the

Table 4. Age, metallicity and abundance ratio of  $\alpha$ -elements ( $[\alpha/\text{Fe}]$ ) derived for the GCs and the central ( $R_{\text{eff}}/8$ ) region of NGC 1407.

ID	PCA <sup>a</sup>		$\chi^2$ <sup>b</sup>		Mg, Fe and Balmer lines <sup>c</sup>		
	[m/H]	Age(Gyr)	[Z/H]	$[\alpha/\text{Fe}]$	Age(Gyr)	[Z/H]	$[\alpha/\text{Fe}]$
GC#01	$-0.81 \pm 0.03$	$10.6 \pm 0.6$	$-0.78 \pm 0.03$	$+0.33 \pm 0.04$	$12.6 \pm 1.3$	$-0.85 \pm 0.06$	$+0.41 \pm 0.03$
GC#03	$-0.22 \pm 0.07$	$13.3 \pm 1.6$	$-0.33 \pm 0.04$	$+0.32 \pm 0.06$	$14.9 \pm 1.5$	$-0.36 \pm 0.03$	$+0.60 \pm 0.18$
GC#04	$-0.69 \pm 0.05$	$11.2 \pm 0.7$	$-0.65 \pm 0.04$	$+0.22 \pm 0.05$	$13.2 \pm 1.6$	$-0.70 \pm 0.07$	$+0.41 \pm 0.04$
GC#05	$-0.50 \pm 0.06$	$3.6 \pm 0.7$	$-0.08 \pm 0.06$	$+0.23 \pm 0.05$	$5.9 \pm 0.8$	$-0.26 \pm 0.07$	$+0.38 \pm 0.04$
GC#06	$-0.78 \pm 0.05$	$11.2 \pm 1.2$	$-0.93 \pm 0.06$	$+0.19 \pm 0.07$	$11.1 \pm 1.1$	$-0.91 \pm 0.04$	$+0.17 \pm 0.05$
GC#07	$-0.41 \pm 0.07$	$4.7 \pm 1.5$	$-0.20 \pm 0.14$	$+0.16 \pm 0.06$	$3.5 \pm 0.8$	$-0.21 \pm 0.09$	$+0.25 \pm 0.04$
GC#08	$-1.01 \pm 0.09$	$10.0 \pm 1.5$	$-1.03 \pm 0.08$	$+0.13 \pm 0.15$	$11.7 \pm 1.7$	$-1.10 \pm 0.07$	$+0.49 \pm 0.13$
GC#09	$-1.44 \pm 0.06$	$8.4 \pm 0.9$	$-1.35 \pm 0.06$	$-0.07 \pm 0.19$	$10.5 \pm 2.4$	$-1.57 \pm 0.15$	$-0.10 \pm 0.18$
GC#11	$-0.27 \pm 0.10$	$11.9 \pm 1.1$	$-0.43 \pm 0.05$	$+0.14 \pm 0.09$	$11.8 \pm 1.6$	$-0.43 \pm 0.07$	$+0.34 \pm 0.08$
GC#12	$+0.03 \pm 0.10$	$9.4 \pm 2.6$	$+0.00 \pm 0.09$	$+0.20 \pm 0.07$	$10.1 \pm 1.5$	$+0.02 \pm 0.07$	$+0.24 \pm 0.05$
GC#13	$-0.82 \pm 0.08$	$8.4 \pm 2.0$	$-0.70 \pm 0.12$	$+0.16 \pm 0.08$	$11.4 \pm 1.4$	$-0.83 \pm 0.06$	$+0.33 \pm 0.08$
GC#14	$+0.12 \pm 0.08$	$11.9 \pm 1.6$	$-0.18 \pm 0.05$	$+0.26 \pm 0.05$	$13.0 \pm 1.8$	$-0.12 \pm 0.04$	$+0.48 \pm 0.04$
GC#15	$-0.31 \pm 0.09$	$8.4 \pm 1.5$	$-0.23 \pm 0.06$	$+0.37 \pm 0.08$	$13.4 \pm 1.5$	$-0.33 \pm 0.04$	$+0.50 \pm 0.02$
GC#17	$-0.08 \pm 0.07$	$14.1 \pm 2.0$	$-0.18 \pm 0.05$	$+0.42 \pm 0.05$	$8.3 \pm 2.6$	$-0.15 \pm 0.07$	$+0.49 \pm 0.04$
GC#18	$-0.29 \pm 0.10$	$15.0 \pm 2.3$	$-0.35 \pm 0.07$	$+0.28 \pm 0.07$	$12.3 \pm 1.5$	$-0.30 \pm 0.05$	$+0.29 \pm 0.06$
GC#22	$+0.35 \pm 0.10$	$9.4 \pm 3.1$	$+0.15 \pm 0.12$	$+0.25 \pm 0.07$	$10.2 \pm 2.2$	$+0.06 \pm 0.10$	$+0.26 \pm 0.05$
GC#26	$-1.10 \pm 0.07$	$11.2 \pm 1.1$	$-1.05 \pm 0.05$	$+0.41 \pm 0.11$	$11.4 \pm 2.1$	$-1.21 \pm 0.08$	$+0.50 \pm 0.12$
GC#27	$+0.24 \pm 0.11$	$12.6 \pm 2.0$	$+0.00 \pm 0.06$	$+0.32 \pm 0.07$	$12.7 \pm 1.6$	$+0.01 \pm 0.06$	$+0.60 \pm 0.13$
GC#30	$-0.12 \pm 0.18$	$7.9 \pm 3.3$	$-0.20 \pm 0.13$	$+0.29 \pm 0.13$	$9.7 \pm 2.1$	$-0.14 \pm 0.07$	$+0.52 \pm 0.09$
GC#33	$-0.96 \pm 0.13$	$3.2 \pm 1.8$	$-0.55 \pm 0.28$	$+0.26 \pm 0.19$	$5.2 \pm 1.7$	$-0.82 \pm 0.14$	$+0.40 \pm 0.14$
$R_{\text{eff}}/8$	...	$11.9 \pm 1.4$	$+0.38 \pm 0.04$	$+0.33 \pm 0.01$	$12.0 \pm 0.4$	$+0.33 \pm 0.03$	$+0.34 \pm 0.01$

Note. — Values derived using different techniques: (a) Metallicity calibration based on a principal component analysis of Lick indices (Strader & Brodie 2004); (b) Multivariate analysis of Lick indices (Proctor et al. 2004); (c) Weighted combination of solutions driven from single index-index diagrams based on  $\text{Mgb}$ ,  $\langle \text{Fe} \rangle$ ,  $[\text{MgFe}]$  and the Balmer Lick indices

indices involved.

According to this method, Figure 7 represents the ages, metallicities and  $[\alpha/\text{Fe}]$  ratios derived for our 20 GCs (filled circles), the  $R_{\text{eff}}/8$  central spectrum of NGC 1407 (filled star), and the sample of 41 GGC spectra (open squares) from Schiavon et al. (2005). Histograms of the three parameters are provided for both GC samples.

The parameters inferred for GGCs allow us to constrain the reliability of the method. In the age-[Z/H] plane of Fig. 7, MP GGCs tend to be younger than MR ones, whereas no such an age-metallicity relationship is known to exist on the basis of accurate CMDs (e.g. de Angeli et al. 2005). Such a fictitious trend might be an artifact of the SSP models that, accounting for BHB effects for  $[\text{Z}/\text{H}] \leq -0.5$ , make the Balmer line strengths to turn up for ages older than  $\sim 9$  Gyr. The old-age regimes of Balmer index-index diagrams thus become bi-valuated and objects with low Balmer indices that lie below the model grids are systematically assigned to be younger than if they were interpreted on the basis of non-BHB effect models. Probably, this inconsistency is in turn driving the extremely large  $[\alpha/\text{Fe}]$  values obtained for GGCs at the low metallicity end. Because of the above limitation, and given that typical uncertainties in dating old stellar populations are in general very large, trying to distinguish small differences among the ages of *old* GCs in NGC 1407 is beyond the scope of this paper. Fortunately, our GC set does not reach [Z/H] values as low as the GGCs and the derived  $[\alpha/\text{Fe}]$  values are still expected to be reasonable.

Keeping in mind the systematic trends introduced by the procedure, it is clear from Fig. 7 that most GCs in NGC 1407 are found to be old like GGCs ( $\sim 11$  Gyr). However 3 of them (GC#05, #07 and #33, see Table 4) formally have ages of  $\sim 4$  Gyr. We defer to Section 7.1 a discussion on the existence of these potentially young GCs (hereafter yGCs) in NGC 1407. For the old GCs only, we compute a mean age of  $10.9 \pm 0.5$  Gyr and a *rms* standard deviation of 2.1 Gyr. Many of them follow the same, fictitious age-metallicity trend as GGCs, although a few GCs with large error bars look slightly younger. In agreement with the metallicities derived according to the PCA method, we find that the GCs in NGC 1407 range from  $[\text{Z}/\text{H}] \sim -1.5$  dex to slightly above solar. For the  $[\alpha/\text{Fe}]$  ratios, we find most GCs have  $\alpha$ -enhanced chemical compositions. In particular, the mean  $[\alpha/\text{Fe}]$  ratio for the whole sample is  $+0.24 \pm 0.03$  dex with a *rms* standard deviation of 0.11 dex. Unlike Puzia et al. (2005), we do not detect any significant correlation between  $[\alpha/\text{Fe}]$  and any of the other two parameters. Finally, the integrated,  $R_{\text{eff}}/8$  central spectrum of NGC 1407 is found to be old ( $11.9 \pm 1.4$  Gyr), metal-rich ( $[\text{Z}/\text{H}] = +0.38 \pm 0.04$  dex) and  $\alpha$ -enhanced ( $[\alpha/\text{Fe}] = +0.33 \pm 0.01$  dex).

### 5.2.2. Using an iterative procedure based on $Mg$ , $Fe$ and Balmer indices

In addition to the above procedure, we carried out an iterative method to determine the ages, metallicities and  $[\alpha/Fe]$  ratios of our GCs and galaxy spectra according to index-index diagnostics based on the Balmer Lick indices ( $H\delta_A$ ,  $H\delta_F$ ,  $H\gamma_A$ ,  $H\gamma_F$  and  $H\beta$ ) as well as  $[MgFe]'$ ,  $Mgb$  and  $\langle Fe \rangle$ . A similar procedure is carried out in Puzia et al. (2005).

Figure 8 illustrates the age-metallicity- $[\alpha/Fe]$  diagnostic diagrams constructed on the basis of the above indices. To follow the location of the three yGCs inferred in Section 5.2.1, different symbols are assigned: circles (old GCs) and triangles (yGCs). In turn, an additional color code is employed to distinguish blue GCs ( $B - I < 1.87$ ; black-filled symbols) from red GCs ( $B - I > 1.87$ ; open and grey-filled symbols, see below). The star corresponds to the  $R_{\text{eff}}/8$  central spectrum of NGC 1407 and, for comparisons, asterisks represent the sample of 41 GGCs of Schiavon et al. (2005).

In panel *a*, model predictions for  $Mgb$  and  $\langle Fe \rangle$  at fixed age (11 Gyr) and varying metallicity (dashed lines) and  $[\alpha/Fe]$  ratios (different-width solid lines) are over-plotted. In particular, red GCs with high  $[\alpha/Fe]$  ratios ( $> 0.4$  dex; GC#03, #14, #15, #17, #27 and #30; see last column in Table 4) are displayed as open circles to allow following their locations throughout different diagnostic diagrams. Hereafter, we will refer to them as  $\alpha$ GCs. The rest of GCs roughly reproduce typical  $[Mg/Fe]$  values of GGCs. In particular, we will refer as *non- $\alpha$* GCs to those red GCs with typical GGC  $[Mg/Fe]$  ratios (grey-filled symbols).

Panels *b – f* display the model predictions with constant  $[\alpha/Fe]$  ratio ( $= +0.3$ ) and varying age (dotted lines) and metallicity for the Balmer Lick indices and  $[MgFe]'$ . The latter is employed as metallicity indicator since, on the basis of TMB03 models, it is defined to be insensitive to different  $[\alpha/Fe]$  ratios. To guide the eye, the 15 Gyr line is represented as a solid line and the solar-metallicity one as dash-dotted line. It is clear from the figure that the GCs in NGC 1407 basically follow an old-aged, metallicity sequence and exhibit  $[\alpha/Fe]$  ratios larger than solar. Also, the Balmer indices of yGCs are systematically larger than those of other GCs with similar  $[MgFe]'$  values –especially in the  $H\delta$  and  $H\gamma$  diagrams (panels *b – e*), thus providing support to the age differences reported in Section 5.2.1.

The ultimate aim of this method is to find, for each object, the best solution of age, metallicity and  $[\alpha/Fe]$  inferred on the basis of two diagnostic diagrams: i) the plane  $Mgb$  vs  $\langle Fe \rangle$  (panel *a*), and ii) the plane  $H_\chi - [Mg/Fe]'$ , where  $H_\chi$  refers to one of the five possible Balmer line indices (panels *b, c, d, e* and *f*). In this sense, by performing this technique for each Balmer line index, five different solutions of age, metallicity and  $[\alpha/Fe]$  are obtained. In particular, for a certain Balmer index, the iterative procedure carried out to infer the final solutions can be summarized in the following diagnostic sequence: 1)  $Mgb - \langle Fe \rangle$  ( $\text{age}_0$ );

2)  $H_\chi - [\text{Mg}/\text{Fe}]'$  ( $[\alpha/\text{Fe}]_1$ ); 3)  $\text{Mgb} - <\text{Fe}>$  ( $[\text{Z}/\text{H}]_2$ ); 4)  $H_\chi - [\text{Mg}/\text{Fe}]'$  ( $\text{age}_3$ ); 5)  $\text{Mgb} - <\text{Fe}>$  ( $[\text{Z}/\text{H}]_4$ ); and 6)  $H_\chi - [\text{Mg}/\text{Fe}]'$  ( $[\alpha/\text{Fe}]_5$ ). For each diagnostic diagram of the sequence, the models are displayed at a fixed parameter –quoted within parenthesis– that corresponds, as indicated in the subscript, to the solution derived in the previous step. An  $\text{age}_0$  of 11 Gyr was assumed as starting point of the sequence. The plane  $\text{Mgb} - <\text{Fe}>$  at fixed  $[\alpha/\text{Fe}]$  was deliberately avoided within the sequence given that it is completely degenerate. Instead, steps 3 and 2 are respectively repeated in 5 and 6 to close the cycle. No grid extrapolations were applied. Instead, for objects lying outside the models, the closest<sup>4</sup> point of the grid was considered as the most reliable solution. In all cases, the method converged after two iterations. If no consistent solutions between the two panels could be found, means of the two different determinations of age,  $[\text{Z}/\text{H}]$  and  $[\alpha/\text{Fe}]$  were computed as final values.

For each object, errors in the ages, metallicities and  $[\alpha/\text{Fe}]$  ratios were estimated according to its index errors by performing MonteCarlo simulations on the model grids. In turn, large extrapolated uncertainties were assigned to those objects falling outside the models. The final ages, metallicities and  $[\alpha/\text{Fe}]$  ratios obtained for each object are listed in Table 4 and correspond to error-weighted means of the five solutions derived from the five different sequences. The final errors in this table were computed as the larger of either the typical error of the error-weighted mean or the error-weighted standard deviation of the five single determinations.

Concerning the  $R_{\text{eff}}/8$  central spectrum of NGC 1407, the current method confirms the results given in the previous section that the galaxy is old, metal rich and  $\alpha$ -enhanced (see values in Table 4). The ages derived here for the galaxy are at odds with the  $\sim 2$  Gyr reported by Denicoló et al. (2005) on the basis of  $\text{H}\beta$ . The reasons for such a discrepancy seem to arise from the emission corrections of  $\text{H}\beta$  computed in that paper since, as pointed out by the authors, they are systematically larger than the ones presented in previous work. We do not find any significant evidence for emission filling  $\text{H}\beta$ , so the index value we employ in this paper is not corrected for emission. Interestingly, the  $\text{H}\delta$  and  $\text{H}\gamma$  Lick indices we have measured for the galaxy are fully consistent (within the errors) with the ones given by Denicoló et al., but they did not use them for age estimations. Finally we note that Thomas et al. (2005) have also published a central age for NGC 1407 using the same SSP models as here and estimate a relatively old age of  $7.4 \pm 1.8$  Gyr. On the basis of surface brightness fluctuations, Cantiello et al. (2005) also reported an age of  $\sim 11$  Gyr for NGC 1407.

---

<sup>4</sup>The minimum distance between a given point and the model grids has been computed taken into account the errors of the indices, that is, by using a re-scaled space in which errors in both axes have the same size.

### 5.3. Age, metallicity and $[\alpha/\text{Fe}]$ ratio comparisons

Figure 9 illustrates a comparison between the ages, metallicities and  $[\alpha/\text{Fe}]$  ratios derived from the different approaches performed in Sections 5.1 and 5.2

In panel *a*, the metallicities derived from the PCA calibration are compared with those obtained from the  $\chi^2$  procedure. For old GCs (filled circles), there exists a total agreement in the low metallicity regime that progressively turns into a small offset ( $\sim 0.12 \pm 0.03$  dex) for metallicities larger than  $-0.5$  dex. As mentioned in Section 5.1, we suspect that the PCA metallicities are overestimated in this regime because of the lack of very metal-rich (MR) GGCs constraining the metallicity calibration. Differences in the mean  $[\alpha/\text{Fe}]$  values of both GC sets could also be driving the observed offset, although issues concerning the definition of the metallicity scales should not be ruled out either. Finally, the three yGCs (open triangles) systematically deviate from the 1:1 relationship as a consequence of the age-metallicity degeneracy. If, as we will discuss later, yGCs were old GCs hosting BHBs, the PCA metallicities derived for these clusters would be a better estimation of their true metal contents.

In panels *b*, *c* and *d*, the ages, metallicities and  $[\alpha/\text{Fe}]$  ratios derived from the iterative method based on Mg, Fe and Balmer Lick indices are respectively compared with the ones inferred from the  $\chi^2$  procedure. Once again, the agreement in metallicity is very good. With a *rms* standard deviation of  $\sim 0.08$  dex, the Mg-Fe-Balmer diagnostic provides slightly lower values in metallicity (by  $\sim 0.04 \pm 0.02$  dex; see panel *b*), which is a consequence of both the age-metallicity degeneracy and the fact that the ages are, in most cases, found to be slightly older (by  $\sim 0.8 \pm 0.6$  Gyr; panel *c*). Therefore, on the basis of the Mg-Fe-Balmer diagnostic, a mean age of  $11.7 \pm 0.4$  Gyr is obtained for the old GC population, with a *rms* standard deviation of  $\sim 1.6$  Gyr. Interestingly, with ages in the range  $\sim 3 - 6$  Gyr, yGCs are again the *youngest* GCs of the sample. The  $[\alpha/\text{Fe}]$  ratios provided by the Mg-Fe-Balmer procedure are essentially the ones inferred from the  $\text{Mgb-}\langle\text{Fe}\rangle$  plane so, unlike the  $\chi^2$  technique, no other elements/indices constrain the final values. The mean  $[\alpha/\text{Fe}]$  ratio for the whole GC sample is  $0.38 \pm 0.04$  dex (with a *rms* standard deviation of  $0.18$  dex), that is,  $\sim 0.14$  dex larger than the one derived from the  $\chi^2$  procedure (panel *d*). The offsets in the mean ages and  $[\alpha/\text{Fe}]$  ratios derived from both techniques are thus readily explained if we consider that  $\text{H}\delta$  and  $\text{H}\gamma$  indices are predicted to increase with the increasing  $\alpha$ -enhancement (TMK04).

It is worth noting that systematic differences among the values in panels *b*, *c* and *d* are just due to the distinct techniques used to infer ages, metallicities and  $[\alpha/\text{Fe}]$  ratios, as both the data and the SSP model predictions are the same in both cases. In this sense, it should be considered as an additional uncertainty that deserves to be taken into account, as age differences of a few Gyr may suffice to support or rule out different GC formation scenarios.

## 6. C and N-sensitive Lick indices

Having discussed the behavior of  $\alpha$ -elements as a whole, in this section we explore, from a qualitative point of view, the behavior of C and/or N-sensitive Lick indices in our GC set. With this aim, Figure 10 illustrates some interesting diagnostic diagrams, with symbols and models being the same as those presented in Fig. 8. Note that, since the models we are using basically account for enhancement of  $\alpha$ -elements at constant C and N, their predictions must be interpreted in a relative way rather than to constrain C and N absolute abundances.

In panels *a* and *b* we find clear correlations –presumably driven by metallicity– between  $\text{CN}_2$  (measuring the strength of the cyanogen molecule; CN) and the indices  $[\text{MgFe}]'$  and  $\langle\text{Fe}\rangle$ . What is even more remarkable is the striking evidence for CN enhancement in NGC 1407 GCs over the full metallicity range. In particular, at fixed  $[\text{MgFe}]'$  values,  $\text{CN}_2$  indices in NGC 1407 GCs are systematically larger than those of GGCs, with index differences increasing from  $\Delta\text{CN}_2 \sim 0.04$  mag (for MP GCs) up to  $\Delta\text{CN}_2 \sim 0.09$  mag (MR GCs). In fact we note that some MR GCs in NGC 1407 reach –and even go beyond– the  $\text{CN}_2$  values of the galaxy, which, in turn, exhibits a very strong  $\text{CN}_2$  index within  $R_{\text{eff}}/8$  as expected for very massive Es (Sánchez-Blázquez et al. 2003). It is important to note here that the error and *rms* of our  $\text{CN}_2$  correction to the Lick system (see Table 2) are small enough that they should not be responsible for any of the above results.

As reported by Tripicco & Bell (1995), the Fe4668 Lick index (hereafter  $\text{C}_24668$ ) is extremely sensitive to carbon abundance. In fact, as it goes as the square of the C abundance,  $\text{C}_24668$  rises steeply with increasing metallicity and the  $\text{C}_2$  bands may be clear for the most metal-rich systems, with the bands being dominated by other species at the very low metallicity regime. As compared to  $\text{CN}_2$ ,  $\text{C}_24668$  values in NGC 1407 GCs exhibit a quite different behavior (panel *c*). At first sight, it is clear that they are not systematically larger than the model predictions. In addition, both NGC 1407 GCs and GGCs follow a *similar*  $\text{C}_24668$ – $\langle\text{Fe}\rangle$  sequence: at the low-metallicity regime they both are essentially consistent with the models, whilst a larger  $\text{C}_24668$  spread is apparent for MR GCs in NGC 1407. Also, unlike  $\text{CN}_2$ ,  $\text{C}_24668$  is clearly stronger in the galaxy than in their GCs (even in the MR ones). Interestingly, the scatter in  $\text{C}_24668$  exhibited by MR GCs is not random:  $\alpha$ GCs (open circles) also possess larger  $\text{C}_24668$  values. Such a difference in the  $\text{C}_24668$ – $\langle\text{Fe}\rangle$  diagram cannot be explained solely by age effects, since it would require age differences of order a Hubble time, inconsistent with the old GC ages derived on the basis of other Lick indices (Sections 5.2.1 and 5.2.2). Therefore, the most plausible interpretation is that C abundances are driving the observed differences: apart from larger  $[\text{Mg/Fe}]$  ratios,  $\alpha$ GCs possess  $[\text{C/Fe}]$  ratios larger than *non- $\alpha$* GCs. Moreover, given that i) the location of  $\alpha$ GCs in the  $\text{C}_24668$ – $\langle\text{Fe}\rangle$  diagram is similar to the one exhibited by MR GGCs, and ii) *non- $\alpha$* GCs (grey-filled symbols) lie

systematically below the models, one should argue for the existence of C underabundances for *non- $\alpha$* GCs.

In panel *d*, the C-sensitive (CH) G4300 band is plotted versus  $\langle \text{Fe} \rangle$ . Once again,  $\alpha$ GCs –except for the one with the largest errors– exhibit mean G4300 values larger than *non- $\alpha$* GCs which basically trace the locus of GGCs. This behavior provides independent support to the above hypothesis that C is either particularly enhanced in  $\alpha$ GCs or depressed in *non- $\alpha$* GCs. As an obvious consequence, the G4300–C<sub>2</sub>4668 plane in panel *e* exhibits  $\alpha$ GCs populating the high metallicity regime of both C-sensitive indices.

Finally, in order to compare the behaviors of N and C-sensitive indices, CN<sub>2</sub> and C<sub>2</sub>4668 are represented in panel *f*. MP GCs distribute along a linear CN<sub>2</sub>–C<sub>2</sub>4668 sequence with a slope similar to the one predicted by the models, even though there exists a clear offset presumably due to the high CN<sub>2</sub> values previously reported. The picture is different for MR GCs, as they strongly deviate from the trend predicted by the models. In particular, CN<sub>2</sub> in *non- $\alpha$* GCs increases dramatically as C<sub>2</sub>4668 has basically saturated (C underabundances). On the other hand,  $\alpha$ GCs lie systematically closer to the model predictions because of their higher C abundances, although they are still far from following the sequence drawn by MP GCs.

To summarize, we report extremely strong CN bands in the GCs of NGC 1407. Interestingly, we find unprecedented hints for the existence of two MR GC regimes with different abundance patterns for Mg and C. Plausible interpretations on the origin of these subpopulations will be discussed in the next section.

## 7. Discussion

As a result of the analysis and interpretation of Lick indices carried out in the previous section, we conclude that the GC system of NGC 1407 basically follows an old-aged, metallicity sequence, reaching metallicities above solar and exhibiting an enhancement of  $\alpha$ -elements. Overall, these results are in reasonable agreement with previous studies on GC systems of Es (e.g. Puzia et al. 2005). Interestingly, we have also found hints for the existence of younger GCs (the so-called, *y*GCs), as well as evidence for two different abundance patterns among MR GCs in NGC 1407 ( $\alpha$ GCs vs *non- $\alpha$* GCs). We devote the present section to discuss the origin and reliability of these results.

## 7.1. Young GCs or blue horizontal branch effects?

Although the origin of the “second parameter” of GGCs (Sandage & Wallerstein 1960; van den Bergh 1967; Sandage & Wildey 1967) is still a controversial issue (e.g. Lee et al. 1994), there exists a well established consensus that the existence of blue horizontal branch (BHB) morphologies is driven by high ratios between the mass of the He burning core and the total stellar mass. Therefore, mass-loss along the red giant branch (RGB) and/or high He abundances are ideal candidates to explain the observed BHB morphologies. Because of the contribution of luminous, A-type stars with  $T_{\text{eff}} \sim 10000$  K, the integrated spectra of old GCs having BHBs exhibit strong Balmer lines (de Freitas Pacheco & Barbuy 1995; Lee et al. 2000; Maraston & Thomas 2000; Maraston et al. 2003; Schiavon et al. 2004, hereafter SCH04) that may be wrongly interpreted in terms of younger ages. Note also that, although it is not discussed in this paper, a similar effect could arise from the presence of a considerable population of blue straggler stars (e.g Rose 1985; Rose 1994; Xing & Deng 2005). Hence, could it be that the yGCs (#05, #07 and #33) reported in Section 5.2 are, actually, old GCs with BHBs?

### 7.1.1. Metal-poor GCs

In order to address the above question, we first aim to carry out a more detailed comparison between our data and the model predictions used in this paper. Based on the HB morphologies observed in GGCs, the models by TMB03 and TMK04 include BHB effects for metallicities below  $-0.5$ . Bearing this upper limit in mind, and provided the metallicities given in Table 4 for yGCs, only GC #33 can be considered well within the metallicity regime in which BHB effects are being accounted for in the models. Note also that, if a BHB were indeed responsible for the high Balmer lines of this cluster, the metallicities estimated in Section 5.2 would have been overestimated due to the implicit age-metallicity degeneracy of the grids, so the *true* metallicity would still be safe for the sake of comparison. The PCA metallicity could thus be considered as a more reasonable value for this particular case.

In Fig. 8 (panels *b* – *f*), BHB effects are apparent in the model grids as the varying metallicity lines at fixed 15 Gyr (solid lines) lie above the predictions for slightly younger SSPs. Within the  $1\sigma$  error bars, GC #33 (black-filled triangle) is consistent with the solid line of each diagram except for  $H\delta_A$ , although even in this case it is certainly close to that line as well. The fact that most GCs in Fig. 8c lie systematically below the models might suggest that a systematic offset in the  $H\delta_F$  data is artificially reconciling GC #33 with the BHB predictions. However, the excellent agreement between NGC 1407 GCs and GGCs would indeed be difficult to interpret if such an offset existed. In any case, it seems clear

that BHB effects in old stellar populations, as calibrated in TMB03 and TMK04, are able to reproduce the strengths of  $H\beta$ ,  $H\gamma$  and, probably,  $H\delta$  in GC #33.

### 7.1.2. Metal-rich GCs

As reported by Greggio & Renzini (1990), BHBs are not just reserved for MP stellar populations but they are also possible in GCs with metallicities above solar. Based on a comparison between MR GGCs with BHBs (NGC 6388 and NGC 6441) and those with similar metallicities hosting just a red HB (RHB; NGC 6356 and NGC 6637), Puzia et al. (2004) set limits to the effect of BHBs on the five Balmer Lick indices. As pointed out by the authors, such an empirical comparison was just made on a local frame and the existence of more extreme BHB morphologies in extragalactic GCs cannot be ruled out. In order to check whether the low ages derived for the two MR, yGCs (#05 and #07; grey-filled triangles in Fig. 8) may be the by-product of BHB morphologies, we have carried out a similar comparison. Unfortunately, we do not have information about the HB morphologies of the GCs in NGC 1407, so it is formally impossible defining a reference sample of GCs with RHBs. Instead, since  $[\text{Mg}/\text{Fe}]'$  is not affected by BHB effects (Puzia et al. 2004), we have established our reference sample to be all those GCs that i) have the same  $[\text{Mg}/\text{Fe}]'$  values (within the errors) than GCs #05 and #07 ( $\sim 2.45 \text{ \AA}$ ; see Table 3) –thus ensuring the effect of metallicity on each single Balmer line-strength to be the same in both subsamples of GCs–, and ii) have been separately confirmed to be old by the two different approaches described in Section 5.2. The GCs fulfilling the above requirements are #03, #11, #15 and #18, the ones will be referred to as *non-BHB* GCs.

In order to consider the most extreme cases, for each Balmer line we have computed the difference between the highest index value of yGCs and the lowest index value of *non-BHB* GCs. The offsets derived in this way are shown in Table 5 together with the ones computed by Puzia et al. (2004) for GGCs. In all cases, the Balmer index offsets between yGCs and *non-BHB* GCs in NGC 1407 are consistent with the ones existing between BHB and RHB, MR GGCs.

New SSP models accounting for BHB effects in the high-metallicity regime have been recently presented by Maraston (2005). For illustration, the offsets corresponding to a solar metallicity SSP –as predicted by that work– are given in the second row of Table 5. In spite of the fact that Maraston quotes the BHB effect on  $H\beta$  as a relative variation, we have transformed it into an absolute, index offset by assuming the typical  $H\beta$  value of a solar metallicity, 15 Gyr old SSP with  $[\alpha/\text{Fe}] = +0.3$ . Once again, it is clear that they are significantly larger than the ones we measure for our MR, yGCs, thus suggesting that the

existence of BHBs in GCs #05 and #07 cannot be ruled out either.

### 7.1.3. BHB spectral diagnostic

To conclude the present discussion, we make use of the method proposed by SCH04 to identify BHBs in the integrated spectra of GCs. In short, if  $H\delta$ ,  $H\beta$  and any Fe line are measured accurately, the presence of BHB stars in a given GC can be inferred if the age derived from the ratio  $H\delta/H\beta$  is substantially younger than the one indicated just by  $H\beta$ . Basically, the above recipe relies on the fact that BHB stars –similar to blue straggler stars– constitute an extra, hot component in old stellar population that essentially contributes at short wavelengths. In this sense, the relative contribution of BHB stars to the integrated  $H\delta$  is larger than it is for  $H\beta$ . In other words, if one uses SSP model predictions that *do not* account for BHB effects –or even if they do it but it is underestimated–, the ages derived from  $H\delta$  for GCs with BHBs should be younger than the ones derived using  $H\beta$ , whilst should be the same for GCs with RHBs. The last argument also holds for MR GCs, as it is proven in SCH04 for NGC 6388 and NGC 6441 (MR GGCs with BHBs). It is clear however that this technique is model-dependent and different stellar population models may drive different solutions.

Interestingly, the integrated Balmer lines of our *y*GCs exhibit qualitatively the same trend as predicted by SCH04 for GCs with BHB stars. At first sight, it is clear from Fig. 8b – f that the relative differences among the Balmer indices of *y*GCs and old GCs with similar [MgFe]’ values are larger for  $H\delta$  and  $H\gamma$  than for  $H\beta$ . Specifically, the individual ages derived from  $H\beta$  and  $H\delta_A$ <sup>5</sup> as result of the iterative procedure described in Section 5.2 are, respectively,  $10.8 \pm 2.8$  and  $5.1 \pm 1.3$  Gyr (#05),  $9.2 \pm 2.9$  and  $6.6 \pm 2.6$  Gyr (#07), and  $6.0 \pm 3.8$  and  $2.8 \pm 1.6$  Gyr (#33), thus confirming the relative age differences predicted by SCH04. As an additional test, Figure 11 illustrates the  $H\delta_A/H\beta$  versus  $\langle \text{Fe} \rangle$  diagnostic diagram proposed by SCH04 to confirm BHB effects. It is clear that our *y*GCs lie systematically above the cloud of old GCs of the same metallicity. Using for each cluster its corresponding  $[\alpha/\text{Fe}]$  ratio given in Table 4, the ages derived from Figure 11 are  $\sim 3.5$  Gyr (#05),  $\sim 6.0$  Gyr (#07), and  $\sim 1.0$  Gyr (#33). Summarizing, the sequence of ages derived for our *y*GCs on the basis of  $H\beta$ ,  $H\delta_A$  and  $H\delta_A/H\beta$  follow a decreasing trend as predicted by SCH04 for SSPs that host BHB stars.

---

<sup>5</sup>We employ  $H\delta_A$  rather than  $H\delta_F$  since, as mentioned above, the model predictions for  $H\delta_F$  seem to be overestimated as compared to GGCs and our GC set, thus deriving unreliable, extremely old ages in most cases

We therefore conclude that, although we cannot completely reject the possibility that our yGCs are indeed younger than the rest of the GC sample, our results for the yGCs are well explained by both BHB model predictions and BHB line-strength diagnostics. In addition we note that, as compared to genuine young GCs populations found in merger remnant Es (e.g. NGC 3610; Strader et al. 2004), we find the behavior, location and distribution of our yGCs to be quite different. The young GCs found by Strader et al. fall around the MR, young regime of typical index-index, age-metallicity, diagnostic diagrams, thus clearly deviating from the locus of the old, *normal* GCs. Instead, our yGCs span over a wider range of metallicity –in fact, they do not belong to the MR end of GCs in NGC 1407– and they just lie slightly above the sequence of old GCs in panels  $b - f$  of Fig. 8. In addition, unlike the merger remnant NGC 3610 (2–3 Gyr old), the existence of young GCs would be difficult to reconcile with the luminosity-weighted age of  $\sim 10 - 12$  Gyr we find for the  $R_{\text{eff}}/8$  central spectrum NGC 1407.

## 7.2. Element abundance ratios in GCs

In Section 6, we have reported, for the first time, evidence for two distinct chemical compositions among MR GCs in an E galaxy, i.e. a subset of MR GCs have larger [Mg/Fe] and [C/Fe] ratios. Here we discuss possible interpretations for the observed differences on the basis of current theories of chemical evolution.

### 7.2.1. GC formation time-scales

Since different elements are preferentially produced by stars of different lifetimes, element abundance patterns are essential to constrain the mechanisms and time-scales of star formation in stellar populations. For instance, the fact that  $\alpha$ -elements (e.g. Mg, Si, Ti) are rapidly ejected to the interstellar medium by massive, Type II SNe (Faber et al. 1992; Worthey et al. 1992; Matteucci 1994), whereas Fe is produced in Type Ia SNe a few gigayears later, means high  $[\alpha/\text{Fe}]$  ratios are often interpreted as a fingerprint of rapid star formation events. Elements like C and N, however, can be produced in stars over a wide range of masses by means of different mechanisms (see e.g. Kobayashi et al. 2006). C is a primary element (that is, an element formed by stellar, nuclear fusion) which can be produced by both massive and intermediate-mass stars. Because of uncertainties in the C yield modeling, it is still a matter of debate whether C is mainly produced in massive stars (Carigi 2000; Henry et al. 2000) or in low and intermediate-mass stars (Chiappini et al. 2003). N is known to have a double nature. It is basically a secondary element (an element that requires a pre-

vious seed to be produced) as it is a by-product of the CNO cycle formed at the expense of pre-existing C. In turn, N is also a primary element that may be formed in intermediate-mass stars during the third dredge-up of the AGB (Renzini & Voli 1981), as well as in massive stars due to stellar rotation (Meynet & Maeder 2002).

The large [Mg/Fe] ratios exhibited by  $\alpha$ GCs thus suggest that they could experience a more rapid star formation than that undergone by *non- $\alpha$* GCs. In turn, their larger [C/Fe] abundance ratios might be an additional clue to constrain their formation time-scales, although a definitive interpretation of the observed [C/Fe] ratios is subject to the above debate on the type of stars that preferably produce C. In fact, both scenarios –involving either massive or intermediate-mass stars– could qualitatively reconcile the large [Mg/Fe] and [C/Fe] values in Figs. 8a and 10c as far as star formation in  $\alpha$ GCs were brief enough to prevent Fe to incorporate into the newly formed stars. Interestingly, the fact that  $\alpha$ GCs basically exhibit the largest values of C-sensitive indices (G4300 and C<sub>24668</sub>; Fig. 10e) indicates that their high [C/Fe] ratios cannot be solely driven by a lack of Fe, but a larger C abundance is indeed necessary. The last argument, together with the high [Mg/Fe] ratios, seem to support the hypothesis that a non-negligible amount of the present-day C content of MR GCs in NGC 1407 could be supplied by massive stars during relatively rapid star formation time-scales.

Finally, we note that some metal-poor stars in our Galaxy also exhibit large [Mg/Fe] and [C/Fe] ratios (Kobayashi et al. 2006). Interestingly, as reported in that paper, [Zn/Fe] may be the clue to constrain the mechanisms driving the above trend: hypernovae, SNe II, or even external enrichment from a binary companion (Suda et al. 2004).

### 7.2.2. *The puzzle of C and N in GCs*

During the last two decades, our understanding of C and N in GCs has basically relied on the study of the cyanogen molecule. From the pioneering work by Burstein et al. (1984), it was established that the CN feature at  $\sim 4215$  Å was enhanced in M31 GCs with respect to both GGCs and E galaxies. Similar results were reported by Brodie & Huchra (1991) and Ponder et al. (1998) using the CN band at  $\sim 3880$  Å. Intriguingly, Beasley et al. (2004; see also Trager 2003) did not detect systematic differences between the CN<sub>2</sub> indices of M31 GCs and GGCs at any metallicity, although they did still find evidence for CN<sub>2</sub> enhancement in M31 GCs and GGCs with respect to their respective galactic bulges and the family of E galaxies. To date, such a CN *anomaly* (see Trager 2003) has been reported to exist not only for M31 GCs but also for GCs in NGC 3115 (Kuntschner et al. 2002), NGC 3610 (Strader et al. 2003a) and the Fornax dSph (Strader et al. 2003b). It is clearly inferred from Section 6

that NGC 1407 is another case of such an increasingly common phenomenon.

In order to understand the ultimate culprit of CN enhancement, there has been an special effort to disentangle how C and N behave separately. Making use of the NH feature at  $\sim 3360 \text{ \AA}$ , N enhancement has been reported to exist for M31 GCs and GGCs (Ponder et al. 1998; Li & Burstein 2003), leading to the idea that N is mostly responsible for CN variations (Burstein et al. 2004). On the other hand, C is thought to be preferably absorbed into the CO molecule. In fact, Li & Burstein also present evidence for M31 and MW GCs having G4300 indices (CH) similar to Galactic dwarf stars, which suggests that C and N indeed have different formation mechanisms, at least in GCs.

The puzzle of chemical evolution is even more complicated if we take into account that C and N abundances may be linked as a consequence of the CNO cycle. The main nucleosynthesis results concerning low and intermediate-mass stars suggest that C yields decrease with increasing initial metallicity, whereas N yields slightly increase with metallicity, as N is formed by consumption of C and O already present in the stars (Chiappini et al. 2003). If, as stated for M31 GCs, CN enhancements are generically driven by a high N content, the striking CN enhancement in NGC 1407 GCs would indeed be indicative of a N overabundance.

Under this assumption, the above picture that C and N follow opposite trends with metallicity is, at least qualitatively, a reasonable scenario to explain the behavior exhibited by NGC 1407 GCs in the  $\text{CN}_2$ – $\text{C}_24668$  diagram of Fig. 10e (that is, a N–C plane). Compared to MP GCs, MR GCs exhibit a striking N overabundance at the time that C has basically saturated. In other words, the N–C relationship steepens drastically with the increasing metallicity as predicted by the above nucleosynthesis theories. In fact, given that N preferably tends to form CN, C underabundances inferred for *non- $\alpha$* GCs from Fig. 10c could be just an artifact of the existing N overabundance: if most C is consumed to form CN, there should not be much C left to form other carbon molecules like  $\text{C}_2$ . This could be an additional reason for the C saturation exhibited, in general, by MR GCs. Only those MR GCs with intrinsic, high C abundances –that is,  $\alpha$ GCs– possess enough C to increase the strength of their  $\text{C}_24668$  indices (Fig. 10f). Furthermore, this could also explain the fact that whilst *non- $\alpha$* GCs follow the MP GC sequence in Fig. 8a (with  $\alpha$ GCs deviating above),  $\alpha$ GCs follow the MP GC sequence in Fig. 10c (with *non- $\alpha$* GCs deviating below). Even though both diagrams might be essentially the same, MR GCs shift down as a whole in Fig. 10c as a consequence of the increasing efficiency of the CNO cycle with metallicity. In any case, it seems clear that Fig. 10f supports the idea that the mechanisms dominating the formation of C and/or N have been different for MP and MR GCs. The wide variety of  $\text{CN}_2$ / $\text{C}_24668$  ratios in MR GCs contrasts with the tight  $\text{CN}_2$ – $\text{C}_24668$  sequence followed by

MP GCs, for which N and C abundances seem to increase in a parallel way as if they both were tied to the same enrichment mechanism. Actually, the last argument is true not only for the CN<sub>2</sub>–C<sub>2</sub>4668 relationship but also for other index-index diagrams involving different element dependencies, in which MP GCs follow a tighter abundance sequence than MR GCs do.

Interestingly, the observed behavior in NGC 1407 GCs is in qualitative agreement with detailed studies of C and N abundances in individual stars of GGCs. Briley et al. (2004) found that, apart from a strongly anticorrelated relationship between the C depletion and the N enhancement of main sequence stars in the MR GGC 47 Tuc (in turn, similar to the one existing for MR GGC M71 stars), they exhibit C and N abundances similar to those in evolved red giants, thus implying little change in surface abundances. The last result is interpreted as evidence for pollution or accretion events early in the history of the cluster. The existence of bimodality in the CN content of 47 Tuc main sequence stars (CN-strong and CN-weak; Hesser 1978) is still a controversial issue that may shed light on the processes involved in the formation and evolution of C and N in MR GCs. In any case, the similarity among the C and N abundances of dwarfs and giants in MR GGCs contrasts with the well-known relationship between the C depletion and the luminosity of the giant branch of MP GGCs (Suntzeff 1981, Smith et al. 2005), in the sense that the larger the luminosity the larger the C depletion and the N enhancement. In this case, the progressive dredge-up of CNO-processed material from regions close to the H-burning shell within Population II giants is proposed to explain the observed trend.

It seems therefore clear that MP and MR GCs suffer intrinsically different processes that determine their overall C and N abundances, what is in perfect agreement with our findings for NGC 1407 GCs. From the point of view of C and N abundances, a general picture of GC chemical enrichment may be summarized as follows: MP GCs form from a relatively metal-free ISM with no apparent C depletion, as the CNO cycle requires the prior existence of C for it to be effective. The CNO cycle would be carried out during their evolution, thus eventually affecting the C and N of some giant stars and, even more importantly, polluting the ISM with enhanced N and depleted C for subsequent star formation. MR GCs would form from such an enriched ISM that keeps fingerprints of previous CNO processes. Pollution during the early star formation history of the cluster could indeed contribute to emphasize the C–N anticorrelation as well as to increase the variety of [N/C] values among MR GCs. At this point, it is still necessary to understand how MP GCs reach such a striking N enhancement if CNO processes are not effective. Very massive, rotating stars (Meynet & Maeder 2002) or zero-metallicity, 200 – 500 M<sub>⊙</sub> stars that go hypernovae and expel out huge amounts of N, C and other elements in an early Universe (Li & Burstein 2003) may help to explain the existence of primordial N overabundances. Assuming that the nucleosynthesis within these

massive, metal-free stars should not differ much from one to the other, these scenarios could explain not only the existence of early N overabundances but also the fact that N and C in MP GCs follow a well defined sequence. In other words, element enrichment in MP GCs might be driven by a more standard mechanism whereas MR GCs may have undergone a wider variety of enrichment histories.

### 7.2.3. *Different subpopulations of MR GCs?*

One of the most interesting differences among GCs is the relative abundances of Mg and C. Could it be that such a dichotomy in the abundance pattern is a consequence of having undergone different star formation histories? If so, to what extent can they provide us clues to confirm or rule out different GC formation scenarios like, e.g., accretions or mergers? In order to discuss the above questions, we examine whether the MR GCs exhibit differences in their kinematics and/or structural parameters that may support the hypothesis of a distinct origin.

i) *Kinematics.* The existence of asymmetries in the velocity distribution of GC subpopulations, as well as certain rotation patterns, can be a fingerprint of recent GC stripping, accretion or merging scenarios (see e.g. Bekki et al. 2005; Schubert et al. 2007, in preparation). As mentioned in Section 3, no clear rotation has been found for our MR GCs, not even when both MR GC sets are considered separately. In addition, we do not detect RV asymmetries either: the mean, heliocentric RV of  $\alpha$ GCs is  $1799 \text{ km s}^{-1}$  (with a *rms* standard deviation of  $351 \text{ km s}^{-1}$ ), whilst the one for *non- $\alpha$* GCs is  $1815 \text{ km s}^{-1}$  (with a *rms* standard deviation of  $372 \text{ km s}^{-1}$ ). Both values are in perfect agreement with each other, as well as with the heliocentric RV determined for NGC 1407 in Section 3.

ii) *Sizes.* GC sizes are thought to be determined by both the physical conditions of the proto-cluster cloud and subsequent dynamical evolution effects. Nevertheless, as recently stated by H06, some of the GCs belonging to the bright-end, unimodal population in NGC 1407 are analogues of the high-mass GCs in the MW (e.g.  $\omega$  Centauri and M54; Harris 1996) and M31 (G1; Meylan et al. 2001). Ultra-Compact Dwarfs and remnant nuclei of accreted and disrupted dEs are possible candidates to populate this bright GC regime. Thus, could it be that either of the two MR GC subpopulations has an *extragalactic* origin?

In order to test the above hypothesis, we use half-light radii for the GCs from F06. We did not find a significant difference between the mean sizes of  $\alpha$ GCs ( $3.6 \pm 0.9 \text{ pc}$ ) and *non- $\alpha$* GCs ( $3.7 \pm 1.7 \text{ pc}$ ). Although this result could be an artifact of the limited spectroscopic sample we are working with, it is important to note that our data still allows us to reproduce

the typical, mean difference of about 20 percent between MR and MP half-light radii (Kundu & Whitmore 1998; Larsen et al. 2001, Kundu & Whitmore 2001), as already reported in F06 for NGC 1407 GCs.

iii) *Radial distribution.* The surface density profile of MR GCs is steeper than that of MP ones (see review by Brodie & Strader 2006). In other words, the ratio between the number of red and blue GC increases towards the center of the galaxy. Other than this observational feature concerning GC spatial distribution, no other systematic differences between GC subpopulations in Es have been reported so far, in spite of some theoretical simulations of MR GC formation (e.g. through disk-disk major mergers; Bekki et al. 2002) predict the existence of certain structures for the newly formed MR GCs.

Regarding the projected, radial distance to the center of the galaxy ( $r_p$ ), we do not find any hint for  $\alpha$ GCs systematically populating different regions than *non- $\alpha$* GCs. Their mean  $r_p$  values are  $8.5 \pm 2.6$  kpc and  $7.0 \pm 1.2$  kpc respectively, with errors accounting for the *rms* standard deviation of the data. Once again, even though this analysis may be limited by the small number of GCs, it is important to note that we do still find significant differences between the mean  $r_p$  of MP ( $11.6 \pm 1.9$  kpc) and MR GCs ( $7.8 \pm 1.4$  kpc) as a whole.

To summarize, we do not find any differences between  $\alpha$ GCs and *non- $\alpha$* GCs in regard to kinematics, sizes or radial distributions. It seems therefore that, whatever the mechanism driving the different abundance pattern is, it is not due to distinct formation conditions as might be expected in mergers or accretions.

## 8. Summary and conclusions

We present Keck spectroscopic data for a sample of 20 GCs in NGC 1407, a giant E0 dominating the NGC 1407 group of galaxies. Radial velocities (RVs) and a subset of 20 Lick/IDS, line-strength indices have been measured for both the GCs and the  $R_{\text{eff}}/8$  central spectrum of the galaxy. On the basis of these measurements, we have carried out an analysis of the kinematics and stellar population properties (age, overall metallicity and certain element abundance pattern) of both the GCs and the galaxy. Main results are summarized in the following sections.

## 8.1. Kinematics

- i) We determine a mean, heliocentric, radial velocity of  $1769 \pm 70 \text{ km s}^{-1}$  –with an overall *rms* standard deviation of  $313 \text{ km s}^{-1}$ – for the GC subsystem of NGC 1407. No signature of GC rotation is found to be significant, although a larger sample of GCs is demanded to confirm this result. The derived heliocentric radial velocity and central velocity dispersion corresponding to the  $R_{\text{eff}}/8$ , integrated, central spectrum of NGC 1407 are, respectively,  $1785.6 \pm 5.2 \text{ km s}^{-1}$  and  $293.5 \pm 4.1 \text{ km s}^{-1}$ .
- ii) The dispersion of the GC RVs clearly drops with the increasing projected distance. This fact may have important implications on the kind of orbits that the GCs follow within the potential well of the galaxy. In particular, the existence of radial orbits (rather than isotropic orbits) would help to explain the observed trend.

## 8.2. Age, metallicity and element abundance ratios

Making use of the measured Lick indices and the SSP model predictions by TMB03 and TMK04, ages, metallicities and  $[\alpha/\text{Fe}]$  ratios for the GCs and the  $R_{\text{eff}}/8$ , integrated, central spectrum of the galaxy have been derived using two different approaches: i) the  $\chi^2$  procedure by Proctor et al. (2004), and ii) an iterative procedure based on Mg, Fe and Balmer Lick indices (see details in Section 5.2.2). An additional metallicity estimate for the GCs has been obtained using the PCA method of Strader & Brodie (2004). On the basis of the above methods we conclude that:

### 8.2.1. Metallicities

- iii) As expected for a massive E, the GC metallicity distribution ranges from metal-poor to slightly above solar. MP and MR GC subpopulations peak at  $[\text{Z}/\text{H}] \sim -0.9$  and  $\sim -0.2$  dex with *rms* standard deviations of 0.28 and 0.16 dex respectively. The integrated,  $R_{\text{eff}}/8$  central spectrum of NGC 1407 is metal-rich ( $[\text{Z}/\text{H}] \sim +0.35$  dex).

### 8.2.2. Ages

- iv) Most GCs in NGC 1407 are confirmed to be old. Depending on the age-dating method, we obtain mean values of  $10.9 \pm 0.5$  Gyr (with a *rms* standard deviation of 2.1 Gyr) and  $11.7 \pm 0.4$  Gyr (with a *rms* standard deviation of  $\sim 1.6$  Gyr). Analogously, the integrated,

$R_{\text{eff}}/8$  central spectrum of NGC 1407 is also found to be similarly old ( $11.9 \pm 1.4$  Gyr or  $12.0 \pm 0.4$  Gyr).

v) In spite of most GCs being old, both age-dating techniques consistently find evidence for the existence of three, presumably *young* GCs, with mean ages of  $\sim 4$  Gyr. However the BHB spectral diagnostic proposed by SCH04 indicates that these presumably *young* GCs are, actually, old GCs hosting BHB stars.

### 8.2.3. Abundance ratios

vi) GCs in NGC 1407 exhibit an evident overabundance of  $\alpha$ -elements. We find them to have mean  $[\alpha/\text{Fe}]$  ratios of  $\sim +0.31$  dex, although it quite depends on the procedure carried out ( $+0.24 \pm 0.03$  dex, with a *rms* standard deviation of 0.11 dex, or  $0.38 \pm 0.04$  dex, with a *rms* standard deviation of 0.18 dex). For the integrated,  $R_{\text{eff}}/8$  central spectrum of NGC 1407 we derive similar  $[\alpha/\text{Fe}]$  values of  $\sim +0.33$  dex ( $+0.33 \pm 0.01$  and  $+0.34 \pm 0.01$  dex from each different technique).

vii) Concerning single element abundances, we report –for the first time– hints for the existence of two chemically-distinct subpopulations of metal-rich (MR) GCs. Some MR GCs exhibit significantly larger  $[\text{Mg}/\text{Fe}]$  and  $[\text{C}/\text{Fe}]$  ratios as compared to the rest of MR GCs. This is the first evidence for a correlation between Mg and C abundances among extragalactic GCs. The possibility that high  $[\text{Mg}/\text{Fe}]$  and  $[\text{C}/\text{Fe}]$  ratios could be just driven by a Fe depletion has been ruled out, since GCs exhibiting high  $[\text{C}/\text{Fe}]$  ratios indeed populate the high-metallicity regime of C-sensitive index-index diagrams. A true enhancement of their C and Mg content therefore is favored. Different star-formation time-scales have been proposed to explain the intriguing correlation between Mg and C abundances. If this were the case, a non-negligible amount of the present-day C content of MR GCs in NGC 1407 could be supplied by massive stars during relatively short star formation time-scales.

viii) We also find striking CN overabundances over the full GC metallicity range. Interestingly, the behavior of C and N in MP GCs clearly deviates from the one exhibited by MR GCs, qualitatively resembling the existing differences among MP and MR GGCs. In particular, for MR GCs, N increases drastically at the same time that C essentially saturates and becomes clearly depleted as compared to the model predictions. From the point of view of chemical evolution, this may be interpreted as a consequence of the increasing importance of the CNO cycle with increasing metallicity.

ix) The above observational constrains allow us to propose the following scenario for GC chemical enrichment. Assuming a primordial overabundance of N, MP GCs would form

from a relatively metal-free ISM with no apparent C depletion, as the CNO cycle requires the prior existence of C for it to be effective. The CNO cycle would be carried out during their evolution, thus eventually affecting the C and N of some giant stars and, more importantly, polluting the ISM with enhanced N and depleted C for subsequent star formation. MR GCs would form from such an enriched ISM that preserves the previous CNO products. Pollution during the early star formation history of the cluster could indeed contribute to the C–N anticorrelation as well as increasing the variety of [N/C] values among MR GCs. Overall, the data presented in this paper support the idea that element enrichment in MP GCs might be driven by a more standard mechanism whereas MR GCs may have undergone a wider variety of enrichment histories.

### 8.3. GC formation scenarios

x) The fact that the two chemically-distinct subpopulations of MR GCs do not exhibit significant differences in their radial velocities, sizes and projected galactocentric distances is at odds with the hypothesis that any of the two subpopulations could have an *extragalactic* origin such as recent accretion or merger processes. Although we strictly cannot rule out the last possibility, local, intrinsic differences in the chemical composition of protoGCs haloes within the potential well of the main galaxy halo (e.g. Forbes et al. 1997), together with different star formation time-scales, may suffice to account for the observed dichotomy.

xi) Overall, the old ages inferred for the GCs in NGC 1407 are consistent with the idea that both MP and MR GC subpopulations in massive Es were formed at high redshift (Strader et al. 2005). Unfortunately, whether or not the MR subpopulation is slightly (say 2 – 3 Gyr) younger than the MP GCs is still an open question. The difficulty of detecting small age differences among old GC subpopulations has been illustrated in this paper, as BHB effects, different age-dating techniques, systematics of the models, and typical uncertainties in the data may blur the derived results. Larger samples of high-quality GC spectra are strongly demanded to address, from a reliable, statistical point of view, the epochs of GC formation in the Universe.

### Acknowledgments

The authors are indebted to the anonymous referee for very useful comments and suggestions. Gratitude is also due to Juerg Diemand for his work on preliminary cosmological simulations for our GC set, as well as to Lee Spitler for providing us with his GC size mea-

surements. This work has been mainly supported by NSF grants AST 02-06139 and AST 05-07729, and the Spanish research projects AYA2003-01840 and AYA2004-03059. AJC acknowledges financial support from a Spanish Fundación del Amo Fellowship. AJC is a *Juan de la Cierva* Fellow of the Spanish Ministry of Education and Science. The authors wish to recognize and acknowledge the very significant cultural role and reverence that the summit of Mauna Kea has always had within the indigenous Hawaiian community. We are most fortunate to have the opportunity to conduct observations from this mountain.

## REFERENCES

Armandroff, T. E., & Zinn, R. 1988, AJ, 96, 92

Ashman, K. M., & Zepf, S. E. 1992, ApJ, 384, 50

Ashman, K. M., & Zepf, S. E. 2001, AJ, 122, 1888

Beasley, M. A., Baugh, C. M., Forbes, D. A., Sharpless, R. M., & Frenk, C. S. 2002, MNRAS, 333, 383

Beasley, M. A., Brodie, J. P., Strader, J., Forbes, D. A., Proctor, R. N., Barmby, P., & Huchra, J. P. 2004, AJ, 128, 1623

Bekki, K., Forbes, D. A., Beasley, M. A., & Couch, W. J. 2002, MNRAS, 335, 1176

Bekki, K., Beasley, M. A., Brodie, J. P., & Forbes, D. A. 2005, MNRAS, 363, 1211

Bellazzini, M., Ferraro, F. R., & Ibata, R. 2003a, AJ, 125, 188

Bellazzini, M., Ibata, R., Ferraro, F. R., & Testa, V. 2003b, A&A, 405, 577

Briley, M. M., Harbeck, D., Smith, G. H., & Grebel, E. K. 2004, AJ, 127, 1588

Brodie, J. P., & Huchra, J. P. 1990, ApJ, 362, 503

Brodie, J. P., & Huchra, J. P. 1991, ApJ, 379, 157

Brodie, J. P., & Strader, J. 2006, ARA&A, 44, 193

Brough, S., Forbes, D. A., Kilborn, V. A., Couch, W., & Colless, M. 2006, MNRAS, 369, 1351

Burstein, D., Faber, S. M., Gaskell, C. M., & Krumm, N. 1984, ApJ, 287, 586

Burstein, D., Li, Y., Freeman, K. C., Norris, J. E., Bessell, M. S., Bland-Hawthorn, J., Gibson, B. K., Beasley, M. A., Lee, H., Barbuy, B., Huchra, J. P., Brodie, J. P., & Forbes, D. A. 2004, *ApJ*, 614, 158

Cantiello, M., Blakeslee, J. P., Raimondo, G., Mei, S.; Brocato, E., & Capaccioli, M. 2005, *ApJ*, 634, 239

Cardiel, N. 1999, PhD thesis, Universidad Complutense, Madrid

Carigi, L. 2000, *RevMexAA*, 36, 171

Carretta, E., & Gratton, R. G. 1997, *A&AS*, 121, 95

Cenarro, A. J., Gorgas, J., Vazdekis, A., Cardiel, N., & Peletier, R. F. 2003, *MNRAS*, 339, L12

Cenarro, A. J., Sánchez-Blázquez, P., Cardiel, N., & Gorgas, J. 2004, *ApJ*, 614, L101

Cenarro, A. J., Peletier, R. F., Sánchez-Blázquez, P., Selam, S. O., Toloba, E., Cardiel, N., Falcn-Barroso, J., Gorgas, J., Jimnez-Vicente, J., & Vazdekis, A. 2007, *MNRAS*, 374, 664

Chiappini, C., Romano, D., & Matteucci, F. 2003, *MNRAS*, 339, 63

Cole, S., Lacey, C. G., Baugh, C. M., & Frenk, C. S. 2000, *MNRAS*, 319, 168

Côté, P., Marzke, R. O., West, M. J., & 1998, *ApJ*, 501, 554

Côté, P., Marzke, R. O., West, M. J., & Minniti, D. 2000, *ApJ*, 533, 869

Côté, P., McLaughlin, D. E., Hanes, D. A., Bridges, T. J., Geisler, D., Merritt, D., Hesser, J. E., Harris, G. L. H., & Lee, M. Y. 2001, *ApJ*, 559, 828

Côté, P., West, M. J., & Marzke, R. O. 2002, *ApJ*, 567, 853

Côté, P., McLaughlin, D. E., Cohen J. G., & Blakeslee J. P. 2003, *ApJ*, 591, 850

Denicoló, G., Terlevich, R., Terlevich, E., Forbes, D. A., Terlevich, A., & Carrasco, L. 2005, *MNRAS*, 356, 1440

De Angeli, F., Piotto, G., Cassisi, S., Busso, G., Recio-Blanco, A., Salaris, M., Aparicio, A. & Rosenberg, A. 2005, *AJ*, 130, 116

Diehl, S., & Statler, T. S. 2006, preprint (astro-ph/0606215)

Dirsch, B., Richtler, T., Geisler, D., Forte, J. C., Bassino, L. P., & Gieren, W. P. 2003, AJ, 125, 1908

Elmegreen, B. G., & Efremov, Y. N. 1997, ApJ, 480, 235

Faber, S. M., Worthey, G., & González, J. J. 1992, in IAU Symp. 149, Stellar Populations of Galaxies, ed. B. Barbuy & A. Renzini (Dordrecht: Kluwer), 255

Forbes, D. A., Brodie, J. P., & Grillmair, C. J. 1997, AJ, 113, 1652

Forbes, D. A., Sánchez-Blázquez, P., Phan, A. T. T., Brodie, J. P., Strader, J., & Spitler, L. 2006, MNRAS, 366, 1230 (F06)

de Freitas Pacheco, J. A., & Barbuyk B. 1995, A&A, 302, 718

Gonzálezk J. J. 1993, PhD thesis, University of California, Santa Cruz

Gorgas, J., Faber, S. M., Burstein, D., González, J. J., Courteau, S., & Prosser, C. 1993, ApJS, 86, 153

Greggio, L., & Renzini, A. 1990, ApJ, 364, 35

Harris, W. E. 1996, AJ, 112, 1487

Harris, W. E. 2001, in Star Clusters, ed. L. Labhardt & Binggeli (Berlin: Springer), 223

Harris, W. E., Whitmore, B. C., Karakla, D., Okoń, W., Baum, W. A., Hanes, D., & Kavelaars, J. J. 2006, ApJ, 636, 90

Henry, R. B. C., Edmunds, M. G., & Köppen, J. 2000, ApJ, 541, 660

Hesser, J. E. 1978, ApJ, 223, L117

Ho, L. C., & Filippenko, A. V. 1996, ApJ, 466, L83

Holtzman, J. A., et al. 1992, AJ, 103, 691

Jarrett, T. H., Chester, T., Cutri, R., Schneider, S., Skrutskie, M., & Huchra, J. P. 2000, AJ, 119, 2498

Kissler-Patig, M., Brodie, J. P., Schroder, L. L., Forbes, D. A., Grillmair, C. J., & Huchra, J. P. 1998, AJ, 115, 105

Kobayashi, C., Umeda, H., Nomoto, K., Tominaga, N., & Ohkubo, T. 2006, ApJ, 653, 1145

Kraft, R. P., & Ivans, I. I. 2003, PASP, 115, 143

Kundu, A., & Whitmore, B. C. 1998, AJ, 116, 2841

Kundu, A., & Whitmore, B. C. 2001, AJ, 121, 2950

Kuntschner, H., Ziegler, B. L., Sharples, R. M., Worthey, G., & Fricke, K. J. 2002, A&A, 395, 761

Larsen, S. S., Brodie, J. P., Huchra, J. P., Forbes, D. A., & Grillmair, C. J. 2001, AJ, 121, 2974

Larson, R. B. 1996, in Formation of the Galactic Halo...Inside and Out, ASP Conference Series, Vol. 92, 1996, Heather Morrison and Ata Sarajedini, eds., p. 241

Layden, A. C., & Sarajedini, A. 2000, AJ, 119, 1760

Lee, H., Yoon, S.-J., & Lee, Y.-W. 2000, AJ, 120, 998

Lee, Y., Demarque, P., & Zinn, R. 1994, ApJ, 423, 248

Li, Y., & Burstein, D. 2003, ApJ, 598, 103

Longo, G., Zaggia, S. R., Busarello, G., & Richter, G. 1994, A&AS, 105, 433

Majewski, S. R. 1994, ApJ, 431, L17

Maraston, C., & Thomas, D. 2000, ApJ, 541, 126

Maraston, C., Gregg, L., Renzini, A., Ortolani, S., Saglia, R. P., Puzia, T. H., & Kissler-Patig, M. 2003, A&A, 400, 823

Maraston, C. 2005, MNRAS, 362, 799

Matteucci, F. 1994, A&A, 288, 57

Meylan, G., Sarajedini, A., Jablonka, P., Djorgovski, S. G., Bridges, T., & Rich, R. M. 2001, AJ, 122, 830

Meynet, G., & Maeder, A. 2002, A&A, 390, 561

Miller, B. W., Whitmore, B. C., Schweizer, F., & Fall, S. M. 1997, AJ, 114, 2381

Oke, J. B. 1990, AJ, 99, 1621

Oke, J. B., Cohen, J. G., Carr, M., Cromer, J., Dingizian, A., Harris, F. H., Labrecque, S., Lucinio, R., Schaal, W., Epps, H., & Miller, J. 1995, PASP, 107, 375

Ostrov, P., Geisler, D., & Forte, J. C. 1993, AJ, 105, 1762

Ponder, J. M., Burstein, D., O'Connell, R. W., Rose, J. A., Frogel, J. A., Wu, C.-C., Crenshaw, D. M., Rieke, M. J., & Tripicco, M. 1998, AJ, 116, 2297

Proctor, R. N., Forbes, D. A., & Beasley, M. A. 2004, MNRAS, 355, 1327

Puzia, T. H., Kissler-Patig, M., Thomas, D., Maraston, C., Saglia, R. P., Bender, R., Richtler, T., Goudfrooij, P., & Hempel, M. 2004, A&A, 415, 123

Puzia, T. H., Kissler-Patig, M., Thomas, D., Maraston, C., Saglia, R. P., Bender, R., Goudfrooij, P., & Hempel, M. 2005, A&A, 439, 997

Renzini, A., & Voli, M. 1981, A&A, 94, 175

Rhode, K. L., Zepf, S. E., & Santos, M. R. 2005, ApJ, 630, 21

Richtler, T., Dirsch, B., Gebhardt, K., Geisler, D., Hilker, M., Alonso, M. V., Forte, J. C., Grebel, E. K., Infante, L., Larsen, S., Minniti, D., & Rejkuba, M. 2004, AJ, 127, 2094

Rose, J. A. 1985, AJ, 90, 1927

Rose, J. A. 1994, AJ, 107, 206

Sánchez-Blázquez, P., Gorgas, J., Cardiel, N., Cenarro, A. J., & González, J. J. 2003, ApJ, 590, L91

Sánchez-Blázquez, P., Peletier, R. F., Jiménez-Vicente, J., Cardiel, N., Cenarro, A. J., Falcón-Barroso, J., Gorgas, J., Selam, S. O., & Vazdekis, A. 2006a, MNRAS, 371, 703

Sánchez-Blázquez, P., Gorgas, J., Cardiel, N., & González, J. J. 2006b, A&A, 457, 809

Santos, M. R. 2003, in Extragalactic Globular Cluster Systems:: Proceedings of the ESO Workshop Held in Garching, Germany, 27-30 August 2002, ESO ASTROPHYSICS SYMPOSIA. ISBN 3-540-40472-4. Edited by M. Kissler-Patig. Springer-Verlag, 2003, p. 348

Sandage, A., & Wallerstein, G. 1960, ApJ, 131, 598

Sandage, A., & Wildey, R. 1967, ApJ, 150, 469

Sargent, W. L. W., Schechter, P. L., Boksenberg, A., & Shorridge, K. 1977, *ApJ*, 212, 326

Schiavon, R. P., Rose, J. A., Courteau, S., & MacArthur, L. A. 2004, *ApJ*, 608, L33 (SCH04)

Schiavon, R. P., Rose, J. A., Courteau, S., & MacArthur, L. A. 2005, *ApJS*, 160, 163

Schweizer, F. 1987, in *Nearly Normal Galaxies: From the Planck Time to the Present; Proceedings of the Eighth Santa Cruz Summer Workshop in Astronomy and Astrophysics*, ed. S. Faber, p. 18. New York: Springer-Verlag

Smith, G. H., Briley, M. M., & Harbeck, D. 2005, *AJ*, 129, 1589

Saglia, R. P., Maraston, C., Thomas, D., Bender, R., & Colless, M. 2002, *ApJ*, 579, L13

Strader, J., Brodie, J. P., Schweizer, F., Larsen, S. S., & Seitzer, P. 2003a, *AJ*, 125, 626

Strader, J., Brodie, J. P., Forbes, D. A., Beasley, M. A., & Huchra, J. P. 2003b, *AJ*, 125, 1291

Strader, J., & Brodie, J. P. 2004, *AJ*, 128, 1671

Strader, J., Brodie, J. P., & Forbes, D. A. 2004, *AJ*, 127, 295

Strader, J., Brodie, J. P., Cenarro, A. J., Beasley, M. A., & Forbes, D. A. 2005, *AJ*, 130, 1315

Strader, J., Brodie, J. P., Spitler, L., & Beasley, M. A. 2006, *AJ*, 132, 2333

Strader, J., Brodie, J. P., & Beasley, M. A. 2007, preprint (astro-ph/0701428)

Suda, T., Aikawa, M., Machida, M. N., Fujimoto, M. Y., & Iben, I., Jr. 2004, *ApJ*, 611, 476

Suntzeff, N. B. 1981, *ApJS*, 47, 1

Thomas, D., Maraston, C., & Bender, R. 2003b, *MNRAS*, 343, 279

Thomas, D., Maraston, C., & Bender, R. 2003a, *MNRAS*, 339, 897 (TMB03)

Thomas, D., Maraston, C., & Korn, A. 2004, *MNRAS*, 351, L19 (TMK04)

Thomas, D., Maraston, C., Bender, R., & Mendes de Oliveira, C. 2005, *ApJ*, 621, 673

Toomre, A., & Toomre, J. 1972, *ApJ*, 178, 623

Toomre, A. 1977, in *Evolution of Galaxies and Stellar Populations*, Proceedings of a Conference at Yale University, eds. B. M. Tinsley, R. B. Larson, p. 40. New Haven: Yale University Observatory

Tonry, J. L., Dressler, A., Blakeslee, J. P., Ajhar, E. A., Fletcher, A. B., Luppino, G. A., Metzger, M. R., & Moore, C. B. 2001, *ApJ*, 546, 681

Trager, S. C., Worthey, G., Faber, S. M., Burstein, D., & González, J. J. 1998, *ApJS*, 116, 1

Trager, S. C., Faber, S. M., Worthey, G., & González, J. J. 2000a, *AJ*, 119, 1645

Trager, S. C., Faber, S. M., Worthey, G., & González, J. J. 2000b, *AJ*, 120, 165

Trager, S. C. 2003, preprint (astro-ph/0307069)

Trentham, N., Tully, R. B., & Mahdavi, A. 2006, *MNRAS*, 369, 1375

Trippicco, M. J., & Bell, R. A. 1995, *AJ*, 110, 3035

Valdés, F., Gupta, R., Rose, J. A., Singh, H. P., & Bell, D. J. 2004, *ApJS*, 152, 251

van den Bergh, S. 1967, *PASP*, 79, 460

van den Bergh, S. 1994, in *The Local Group: Comparative and Global Properties*, ESO Conference and Workshop Proceedings, Third CTIO/ESO Workshop on The Local Group, La Serena, Chile, 25-28 January 1994. Edited by Andrew Layden, R. Chris Smith, and Jesper Storm. Garching near Munich: European Southern Observatory, 1994., p.3

Vazdekis, A., Peletier, R. F., Beckman, J. E., & Casuso, E. 1997, *ApJS*, 111, 203

Whitmore, B. C., & Schweizer, F. 1995, *AJ*, 109, 960

Worthey, G. 1992, PhD thesis, University of California, Santa Cruz

Worthey, G., Faber, S. M., & González, J. J. 1992, *ApJ*, 398, 69

Worthey, G., Faber, S. M., González, J. J., & Burstein, D. 1994, *ApJS*, 94, 687 (W94)

Worthey, G., & Ottaviani, D. L. 1997, *ApJS*, 111, 377 (W97)

Xing, Y., & Deng, L. 2005, *ApJ*, 619, 824

Yoon, S-J., Yi, S. K., & Lee, Y-W, 2006, *Science*, 311, 1129

Zepf, S. E., & Ashman, K. M. 1993, MNRAS, 264, 611

Zepf, S. E., Beasley, M. A., Bridges, T. J., Hanes, D. A., Sharpless, R. M., Ashman, K. M., & Geisler, D. 2000, AJ, 120, 2928

Zinn, R., & West, M. J. 1984, ApJS, 55, 45

Table 5. Offsets in the Balmer Lick indices of MR stellar populations due to BHB effects.

	$\Delta H\delta_A$ (Å)	$\Delta H\delta_F$ (Å)	$\Delta H\gamma_A$ (Å)	$\Delta H\gamma_F$ (Å)	$\Delta H\beta$ (Å)
MR GGCs + BHB (Puzia et al. 2004) <sup>a</sup>	2.0	1.0	3.3	1.4	0.4
$[Z/H]_{\odot}$ SSP + BHB (Maraston 2005) <sup>b</sup>	4.8	5.7	2.4	2.9	0.9
MR yGCs in NGC 1407 <sup>c</sup>	$2.15 \pm 0.60$	$1.41 \pm 0.45$	$1.80 \pm 0.49$	$1.69 \pm 0.37$	$0.47 \pm 0.28$

Note. — Offsets in the Balmer Lick indices of: (a) metal-rich GGCs, with offsets arising from the existence of BHB morphologies (Puzia et al. 2004); (b) solar-metallicity, SSP models by Maraston (2005), with offsets accounting for BHB effects; and (c) metal-rich, presumably *young* GCs in NGC 1407 (#05 and #07) as compared to a subsample of metal-rich, old GCs in this galaxy with similar [Mg/Fe]’ values (#03, #11, #15 and #18). The offsets in (c) are comparable to and lower than those in (a) and (b) respectively, so BHB effects cannot be ruled out to explain the large Balmer Lick indices in (c). See more details in the text.

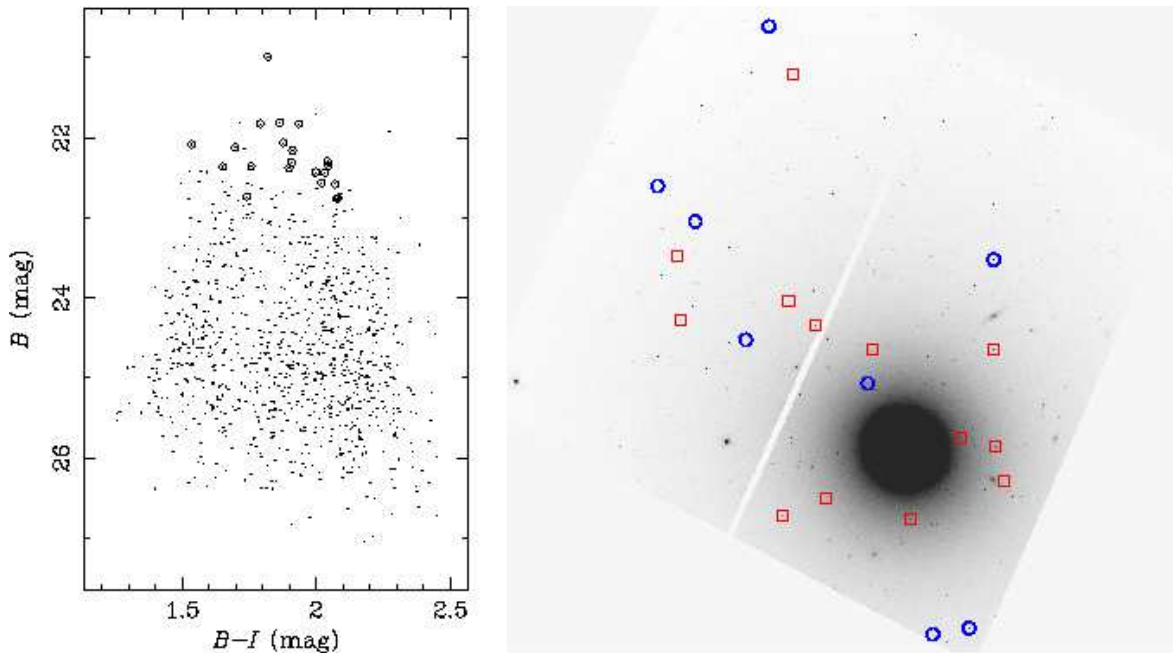


Fig. 1.— *Left*: color-magnitude diagram derived from HST ACS/WFC photometry (Forbes et al. 2006) for the globular cluster candidates of NGC 1407. Each point in the diagram corresponds to a single GC candidate. The 21 circled points indicate those GC candidates that were selected for spectroscopy. *Right*: ACS/WFC imaging of NGC 1407 illustrating the location around the galaxy of the 21 GC candidates for which spectroscopic data were obtained. Circles and squares are displayed for  $B - I < 1.87$  and  $B - I > 1.87$  respectively.

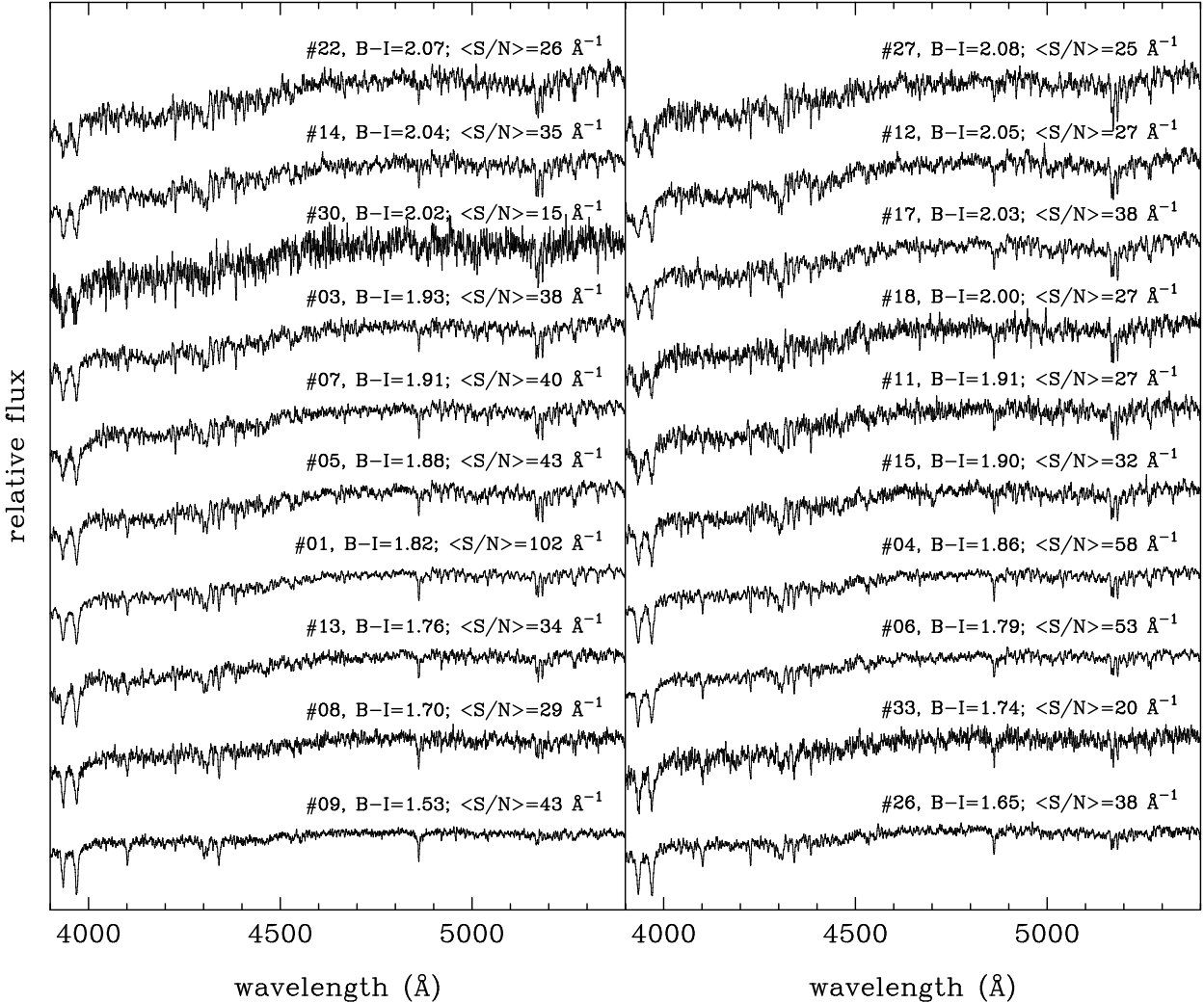


Fig. 2.— Spectra of the 20 GCs in NGC 1407 observed in this work. From bottom to top and from right to left, the GC spectra are displayed following an increasing color sequence. ID numbers,  $B - I$  colors, and mean signal-to-noise ratios per angstrom averaged over the whole spectral range are provided in the labels.

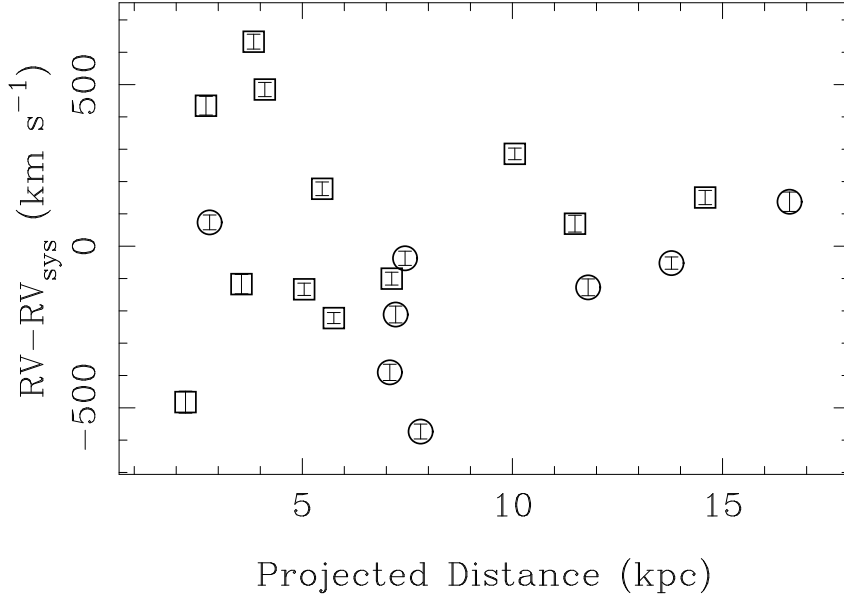


Fig. 3.— Radial velocities of the GCs corrected for the systemic radial velocity ( $RV_{\text{sys}} = 1769 \pm 70 \text{ km s}^{-1}$ ) as a function of the projected distance from the center of NGC 1407. Different symbols represent GCs with  $B - I < 1.87$  (circles; metal-poor) and  $B - I > 1.87$  (squares; metal-rich). A distance of 20.9 Mpc has been assumed for the galaxy (Forbes et al. 2006).

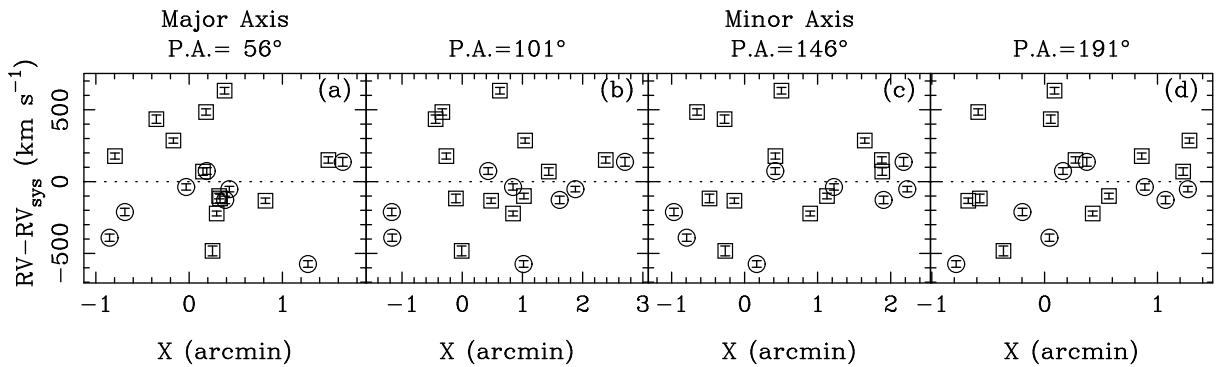


Fig. 4.— Relative radial velocities of the GCs as a function of projected distance to different axis: major axis (a), minor axis (c) and two intermediate directions (b and d). No systematic rotation of the GC system around the galaxy is detected. Symbols as in Fig. 3.

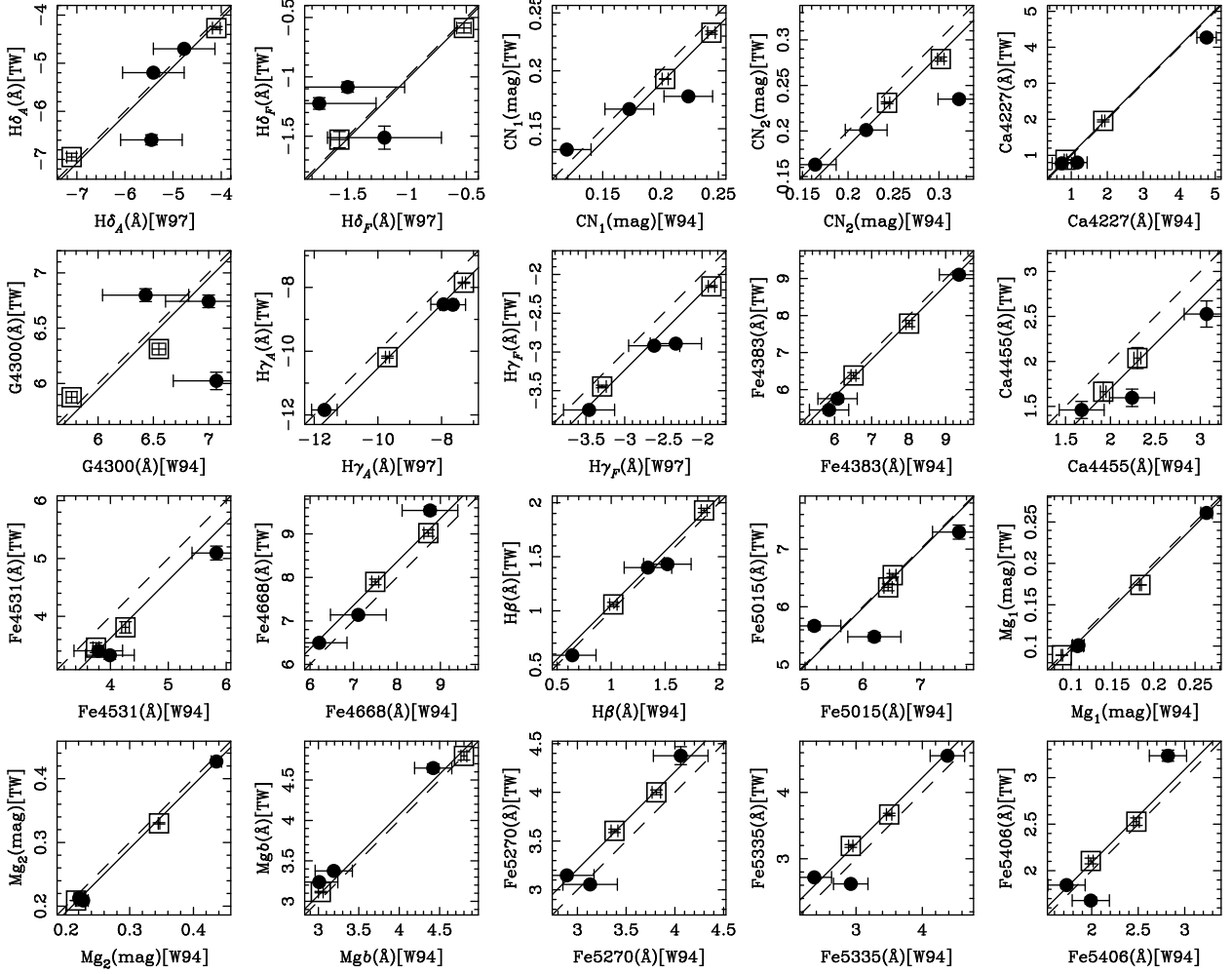


Fig. 5.— Comparison between the Lick indices of five Lick/IDS stars in the Lick system (W94; W97) and those measured in this work (TW) at the spectral resolutions of Table 2. The mean index errors given in W94 and W97 are assumed for HR 2153, HR 2459, and HR 8165 (filled circles). For the Lick stars HR 2002 and HR 7429 (open squares), which have several repeat observations in W94 and W97, their typical errors are used. Dashed lines indicate the 1:1 relation, while solid lines represent the derived, error-weighted offsets between both datasets.

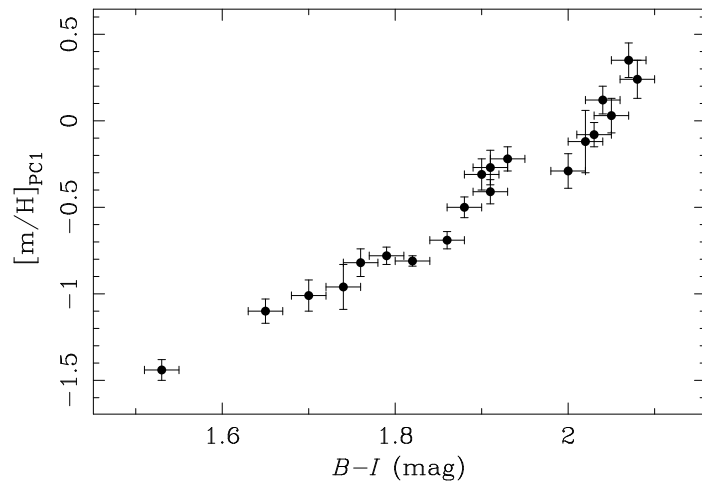


Fig. 6.— Color–metallicity relationship for GCs in NGC 1407. Metallicities are derived from the first component (PC1) of the principal component analysis (PCA) for GGCs by Strader & Brodie (2004).  $B - I$  colors are taken from Forbes et al. (2006; see also Table 1).

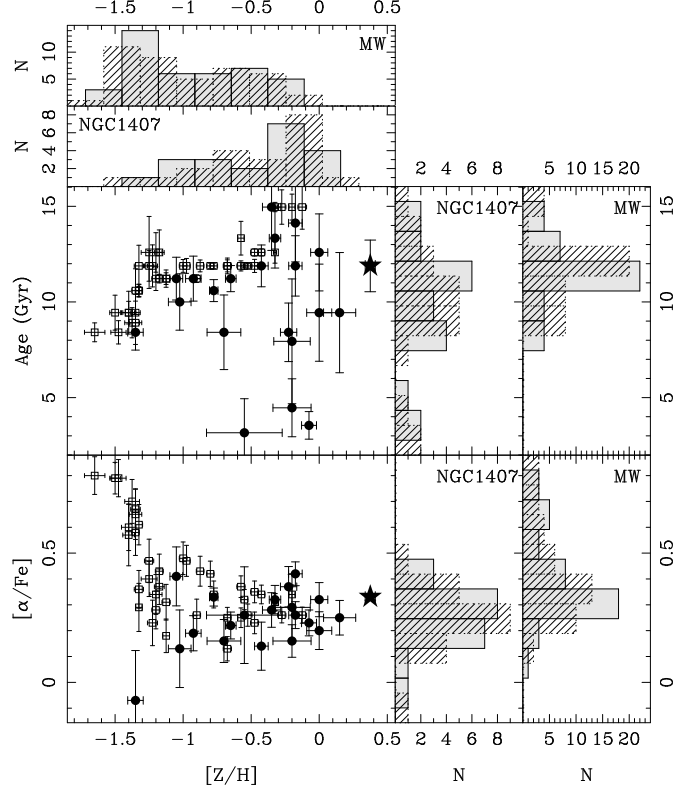


Fig. 7.— Ages, metallicities and  $[\alpha/\text{Fe}]$  ratios for the GCs in NGC 1407 (filled circles) and the central ( $R_{\text{eff}}/8$ ), integrated, galaxy spectrum (filled star) as derived from the  $\chi^2$  procedure by Proctor et al. (2004; see text). Open squares represent the sample of 41 GGCs by Schiavon et al. (2005) which has been analyzed in the same way for the sake of comparison. Histograms of the derived ages, metallicities and  $[\alpha/\text{Fe}]$  ratios are provided for both samples of GCs. In each case, shaded and stripped histograms—shifted half a bin one from the other—account for bin sampling effects.

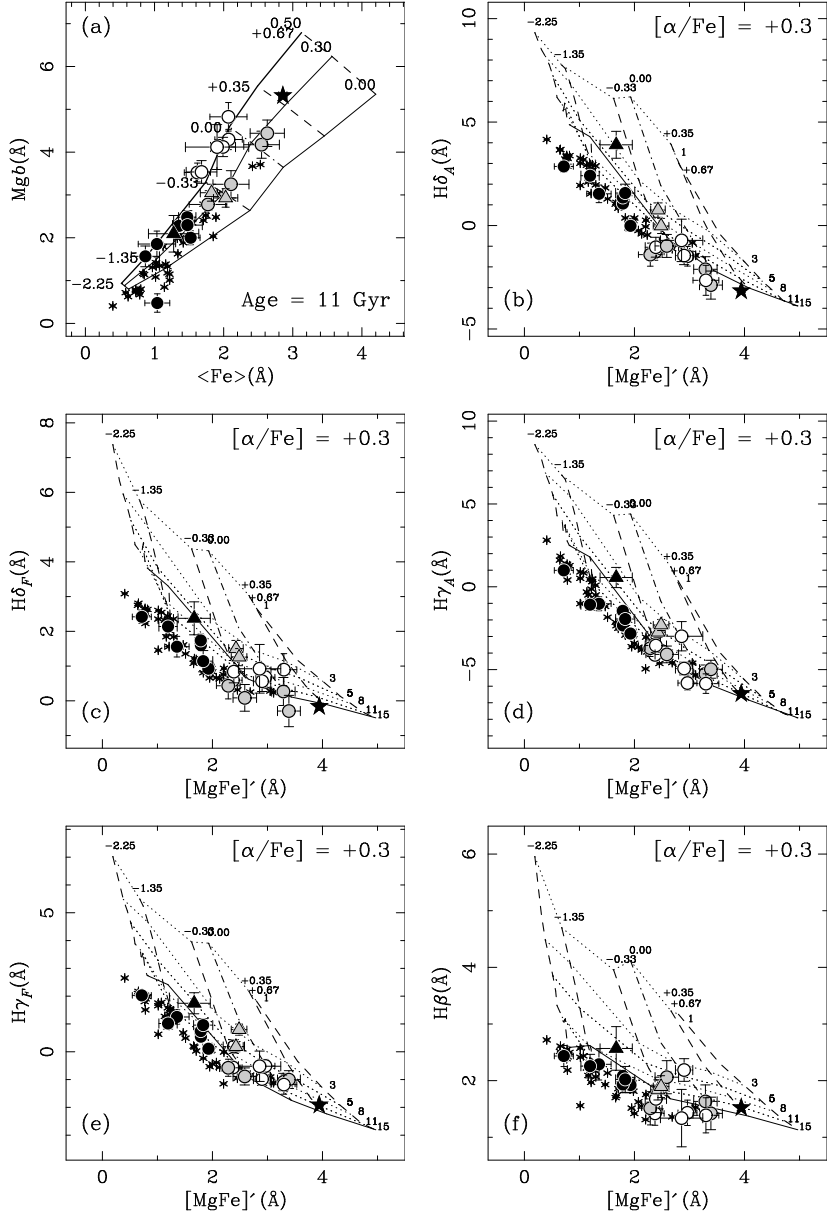


Fig. 8.— Age-metallicity- $[\alpha/\text{Fe}]$  diagnostic plots constructed on the basis of  $\text{Mgb}$ ,  $\langle \text{Fe} \rangle$ ,  $[\text{MgFe}]'$  and the Balmer Lick indices. Circles (both filled and open) and triangles correspond, respectively, to old and *young* GCs (*y*GCs) as derived from the  $\chi^2$  procedure in Section 5.2.1. Metal-poor GCs ( $B - I < 1.87$ ) are illustrated as black-filled symbols, whilst open and grey-filled symbols represent metal-rich GCs ( $B - I > 1.87$ ). The star corresponds to the  $R_{\text{eff}}/8$  central spectrum of NGC 1407. Asterisks represent the sample of 41 GGCs of Schiavon et al. (2005). In panel *a*, model predictions for  $\text{Mgb}$  and  $\langle \text{Fe} \rangle$  at fixed age (11 Gyr) and varying metallicity and  $[\alpha/\text{Fe}]$  ratios (dashed lines and different-width solid lines respectively; see the labels) are over-plotted. In particular, metal-rich GCs with  $[\alpha/\text{Fe}] > 0.4$  dex –as derived from this plane– are displayed as open circles ( $\alpha$ GCs), whilst grey-filled symbols are reserved for the rest of metal-rich GCs (*non- $\alpha$* GCs). Panels *b* – *f* display the model predictions with constant  $[\alpha/\text{Fe}]$  ratio (+0.3) and varying age (dotted lines; see the labels) and metallicity for the Balmer Lick indices and  $[\text{MgFe}]'$ . To guide the eye, the 15 Gyr line is represented as a solid line and the solar-metallicity one as dash-dotted line.

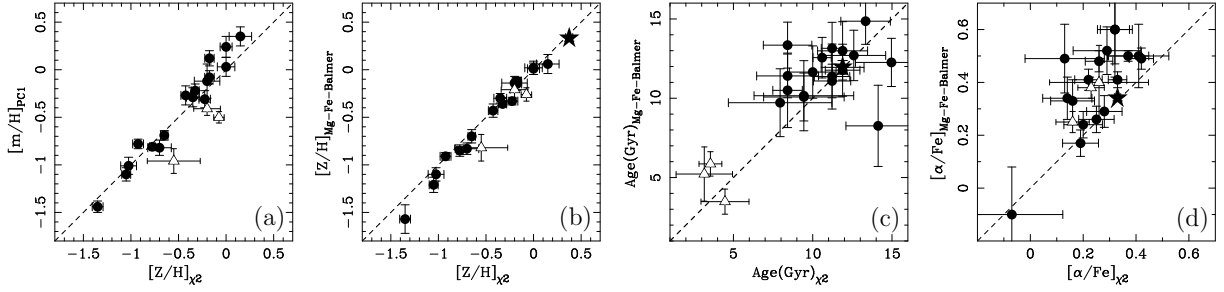


Fig. 9.— Comparison between the ages, metallicities and  $[\alpha/\text{Fe}]$  ratios of the GCs derived from the PCA calibration (Strader & Brodie 2004), the  $\chi^2$  procedure (Proctor et al. 2004) and the iterative procedure based on Mg, Fe and Balmer Lick indices (see details in Section 5.2.2). Open triangles have been used for those presumably young GCs, whereas filled circles represent the remaining of GCs. The central ( $R_{\text{eff}}/8$ ), integrated, galaxy spectrum is represented as a filled star. The dashed line indicates the 1:1 relationship.

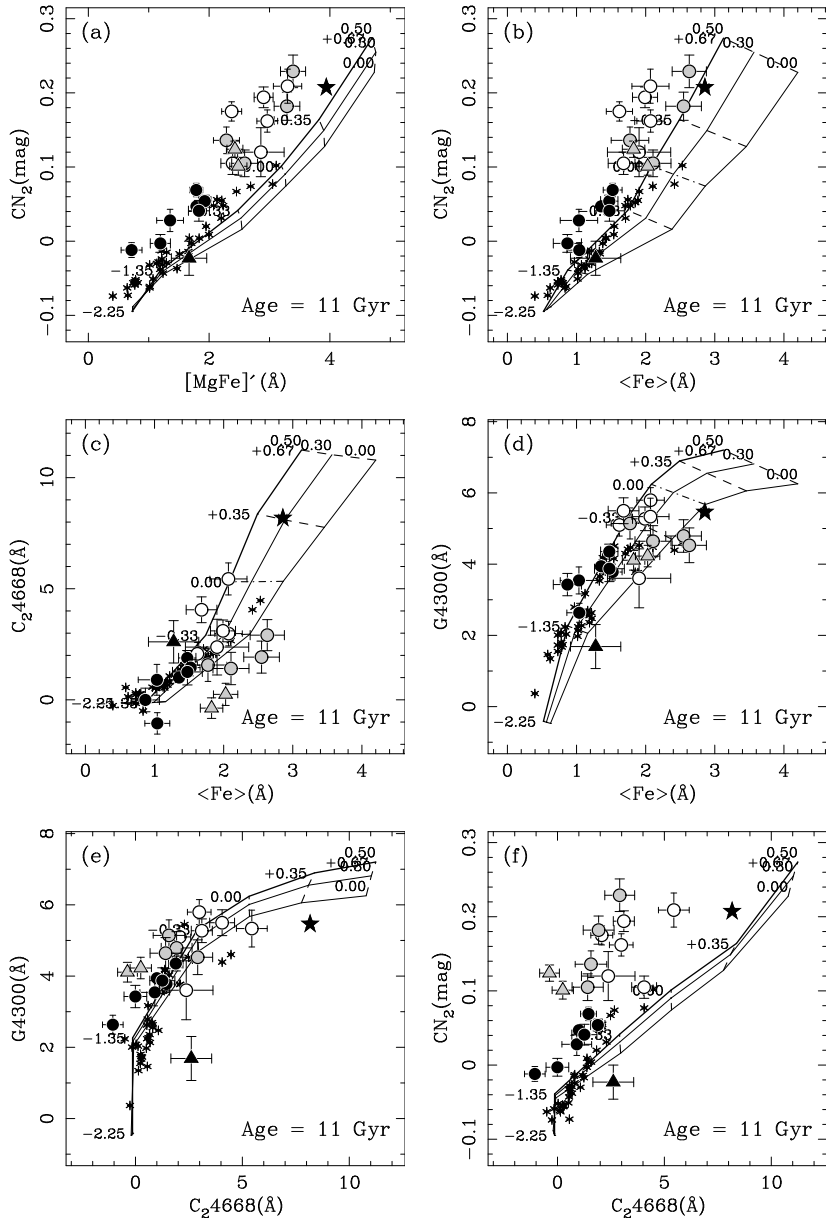


Fig. 10.— Index-index diagnostic diagrams of Lick indices sensitive to C, N, Mg and Fe. Symbols and models as in Fig. 8

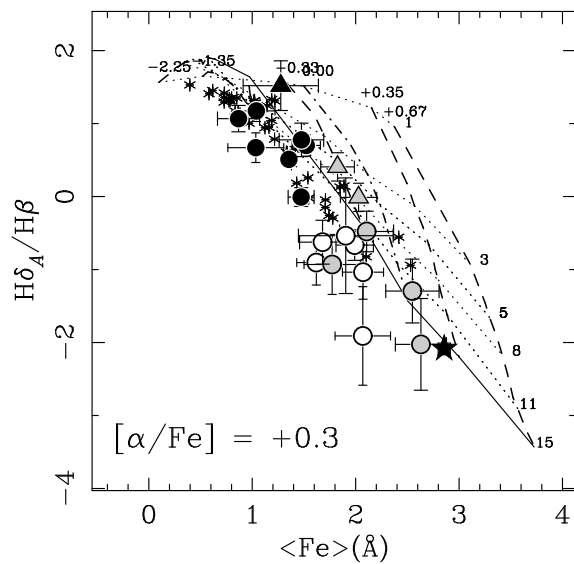


Fig. 11.— Diagnostic diagrams to detect BHB morphologies in the integrated spectra of old GCs as proposed by Schiavon et al. (2004). Symbols and models as in Figure 8.